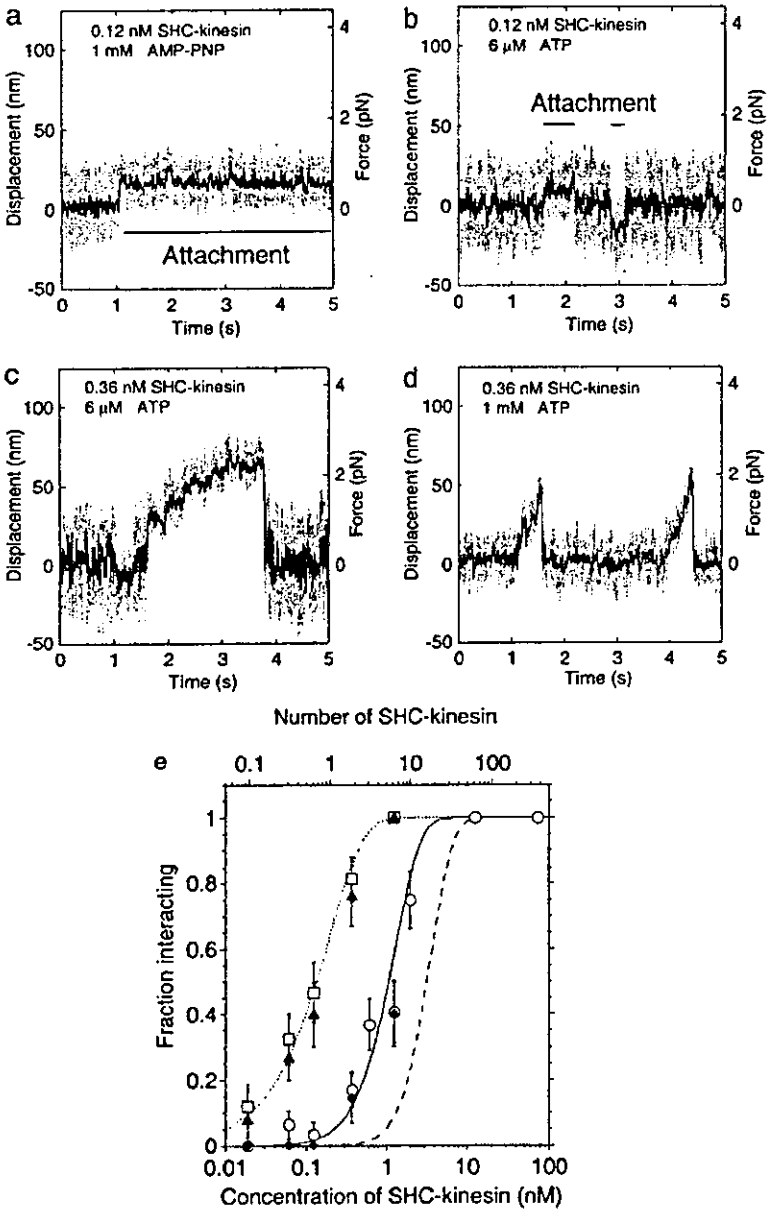

FIGURE 1 Behavior of the SHC-kinesin. (*a–d*) Force generation of SHC-kinesin. Data without low pass filter (*shaded traces*) and having passed through a 50 Hz low pass filter (*black traces*). Attachment in the presence of 1 mM AMP-PNP (*a*) and sequential attachment and detachment at 6 μM ATP (*b*) at SHC-kinesin concentration of 0.12 nM. Continuous movement at 6 μM (*c*) and 1 mM ATP (*d*) at SHC-kinesin concentration of 0.36 nM. (*e*) The ratio of the SHC-kinesin-beads interacting with a microtubule to all beads measured is shown as a fraction of those interacting (*vertical axis*). In this study, an interacting event is when the variance decreased to half its initial value for longer than 50 ms. Rectangles indicate the ratio of the beads binding to microtubules at 1 mM AMP-PNP. Triangles indicate the ratio of the beads interacting with microtubules at 6 μM ATP. The average number of SHC-kinesin molecules on a bead was calculated by fitting the Poisson distribution (*dotted curve*) to the data at 1 mM AMP-PNP and is shown on an upper abscissa. The ratios of the beads moving continuously at 1mM ATP and 6 μM ATP are shown in the circles and diamonds, respectively. Error bars are expressed as $\pm(p(1-p)/n)^{1/2}$, where p is the fraction interacting and n is the number of the measuring beads ($n = 19 \sim 42$ at each point; Svoboda and Block, 1994). The moving ratios were simulated when two or more (*solid curve*) or three or more (*dashed curve*) SHC-kinesin molecules on a bead interacted simultaneously with a microtubule (see Appendix).

interacting with a microtubule increased with an increase in C (Fig. 1 *e*, *rectangles* on the *dotted line*). Therefore, the average number of SHC-kinesins bound to a bead assuming the Poisson distribution of the molecules on beads can be calculated (Fig. 1 *e*, *upper horizontal axis*).

At ATP concentrations of 6 μM, the ratio of the beads interacting with a microtubule was almost the same as that of the beads in the presence of AMP-PNP (Fig. 1 *e*, *triangles* and *rectangles*). At low ATP and low SHC-kinesin concentrations ($<\sim$1 nM), the ratio of the beads moving continuously was considerably lower than that of the beads interacting with a microtubule (Fig. 1 *e*, *triangles* and *diamonds*). This indicates that single molecules of SHC-kinesin bind to and dissociate from a microtubule without processive movement, although multiple molecules can move continuously.

In the presence of 1 mM ATP, the ratio of the beads interacting with a microtubule was lower than that of the beads in the presence of 6 μM ATP (Fig. 1 *e*, *triangles* and *circles*). The time from binding to dissociation (the cycle time) was too short to detect and is discussed later. The ratio of the beads interacting with a microtubule was almost the same as that of the beads moving continuously in the presence of 6 μM ATP (Fig. 1 *e*, *circles* and *diamonds*).

The minimum number of SHC-kinesin molecules required for the continuous movement on a bead was determined by comparing the ratio of the beads moving continuously with

the curves obtained from a simulation model. In this model, the distances among the SHC-kinesin molecules were calculated by considering the geometry of the spherical bead and SHC-kinesin construct and testing whether molecules on the bead interacted simultaneously with the microtubule (see Appendix). The ratio of the continuous movement in the presence of 1 mM ATP (*circles* in Fig. 1 *e*) and the number of interacting molecules was in good agreement with the solid curve (Fig. 1 *e*), which shows that two or more molecules of SHC-kinesin simultaneously interact with a microtubule. The data, however, could not be fitted to the curve that describes three or more molecules of SHC-kinesin interacting with the microtubule (*dashed curve* in Fig. 1 *e*). This result suggests that two molecules of SHC-kinesin are able to support continuous movement.

Binding and dissociation of SHC-kinesin

Single molecules of SHC-kinesin bound to and dissociated from a microtubule without processive movement (Figs. 1 *b* and 2 *a*). The dwell time and the directionality when SHC-kinesin bound to a microtubule were analyzed. The event where the noise (the variance of displacement) was reduced to less than half for >50 ms was considered to be a binding event (Fig. 2 *a*). Time (t_B) from the binding to the dissociation was measured to determine the binding time (Fig. 2 *a*). The histograms of t_B showed an exponential decay with a time constant of 99 ms at 6 μM ATP and 380 ms at 1.2 μM ATP (Fig. 2 *b*).

The histograms of the displacement are shown in Fig. 2 *c*. X_1 and X_2 show the mean displacement from the trap center for a 50 ms period after binding and before dissociation. This allowed the directionality of binding to be measured. The microtubule polarity was determined by marking the minus end with a strong fluorescence dye (Howard and Hyman, 1993). Microtubules with opposite directionalities were selected to minimize any artifacts associated with the shift. The minus ends of 50% of the microtubules were oriented to the upper region on the TV display and the other 50% to the lower region. The histograms of X_1 and X_2 show Gaussian distributions which have peaks biased to the plus end of the microtubule. The values of X_1 and X_2 were 3.4 ± 0.8 nm (mean ± SE, n = 400) and 3.5 ± 0.9 nm (n = 400), respectively. These values did not depend on the direction that the microtubules were oriented on the TV display; the displacements at the opposite directionalities of microtubules were 3.1 ± 1.1 and 3.8 ± 1.1 nm for X_1 and 3.2 ± 1.2 and 3.8 ± 1.1 nm for X_2. The average step size of each bead was 2–6 nm with a standard error of 2 nm (n = 100), indicating that no continuous movement had been included in the steps upon binding. As a result, single molecules of SHC-kinesin bound to a microtubule toward the plus end of the microtubule with a 3.5 nm bias. The displacement from X_1 to X_2, 0.18 ± 0.6 nm (n = 242, $t_B \geq$ 100 ms), was not significantly different from zero (Fig. 2 *c*). Furthermore, the ensemble displacement was analyzed by synchronizing the traces at both binding and detachment (n = 71, t_B > 100 ms; deCastro et al., 2000; Okada et al., 2003). Displacements were considered significant if they were >1.5 (±2 SD) nm within ~3 ms after binding. No such displacements were observed. These results indicate that single molecules of SHC-kinesin bind to microtubules in the direction of the plus end and do not move during binding.

Movement of multiple molecules of SHC-kinesin

The ratio of the beads moving continuously for distances >20 nm after binding to a microtubule (>2 steps of 8 nm) increased with an increase in the concentration of SHC-kinesin. The continuous movement of the SHC-kinesin and the processive movement of double-headed kinesin at the various concentrations are shown in Fig. 3 *a*. The beads coated with SHC-kinesin moved continuously for 70–200 nm and then detached from the microtubule. The frequency of force generation increased as the SHC-kinesin concentration increased from 0.36 nM to 2.0 nM. At an SHC-kinesin concentration of 12 nM, the period when the beads dissociated from the microtubules decreased dramatically. Beads that detached from the microtubule quickly reattached to the microtubule before it had returned to the center of laser trap at zero force and then once again showed continuous movement. Single molecules of double-headed kinesin at a concentration of 0.1 nM moved processively for ~200 nm and generated stall forces of 7–8 pN as reported previously (Inoue et al., 1997; Iwatani et al., 1999).

The histograms of the force generated by SHC-kinesin and double-headed kinesin are shown in Fig. 3 *b*. The force was measured just before kinesin detached from the microtubules. The force population of SHC-kinesin in the histograms decreased almost exponentially with the increase in force. The mean force at an SHC-kinesin concentration of 0.36 nM was 1.7 pN, and this increased to 2.7 pN at a concentration of 12 nM. The force population of double-headed kinesin was increased and then decreased with an increase in the force (*bottom* in Fig. 3 *b*). The stall force, at which kinesin did not move >10 nm over a time frame of 100 ms, was 7 ~ 8 pN. The mean force of 4.9 pN, however, was lower because the forces before movement ceased have been included.

The force-velocity relationships for two molecules of SHC-kinesin at <1.2 nM and for single molecules of double-headed kinesin are shown in Fig. 4 *a*. The highest 10% of forces (>7 pN) for double-headed kinesin which corresponded to the stall force recorded have been analyzed (Iwatani et al., 1999; Kojima et al., 1997). Therefore, the highest 10% of forces were also analyzed for SHC-kinesin. At low forces of ~1pN, the velocity of SHC-kinesin was ~400 nm/s. This value was approximately half of the velocity obtained for double-headed kinesin, ~750 nm/s. The sliding velocity of double-headed kinesin decreased

slightly with forces up to 3 pN and dramatically at forces >3 pN. The sliding velocity of SHC-kinesin decreased in an almost linear fashion.

The force and velocity changed with the concentration of SHC-kinesin (Fig. 4 *b*). The mean force increased gradually from 1.7 to 2.7 pN with an increase in the concentration of SHC-kinesin from 0.36 nM to 12 nM. The velocity of SHC-kinesin was recorded at small forces of ~1 pN. The velocity remained constant at ~350 nm/s at SHC-kinesin concentrations between 0.36 and 2.0 nM and then decreased to ~230 nm/s at a concentration of 12 nM.

DISCUSSION

Nonprocessive movement of single molecules of SHC-kinesin

In this study, the movement of single molecules of SHC-kinesin expressed as monomers (Berliner et al., 1995) was measured by the laser trap and nanometry system. Single and multiple molecules of SHC-kinesin bound to small beads, 0.2 μm in diameter, interacted with a microtubule. The position of the beads was detected with high spatiotemporal resolution to accurately determine the movement of SHC-kinesin.

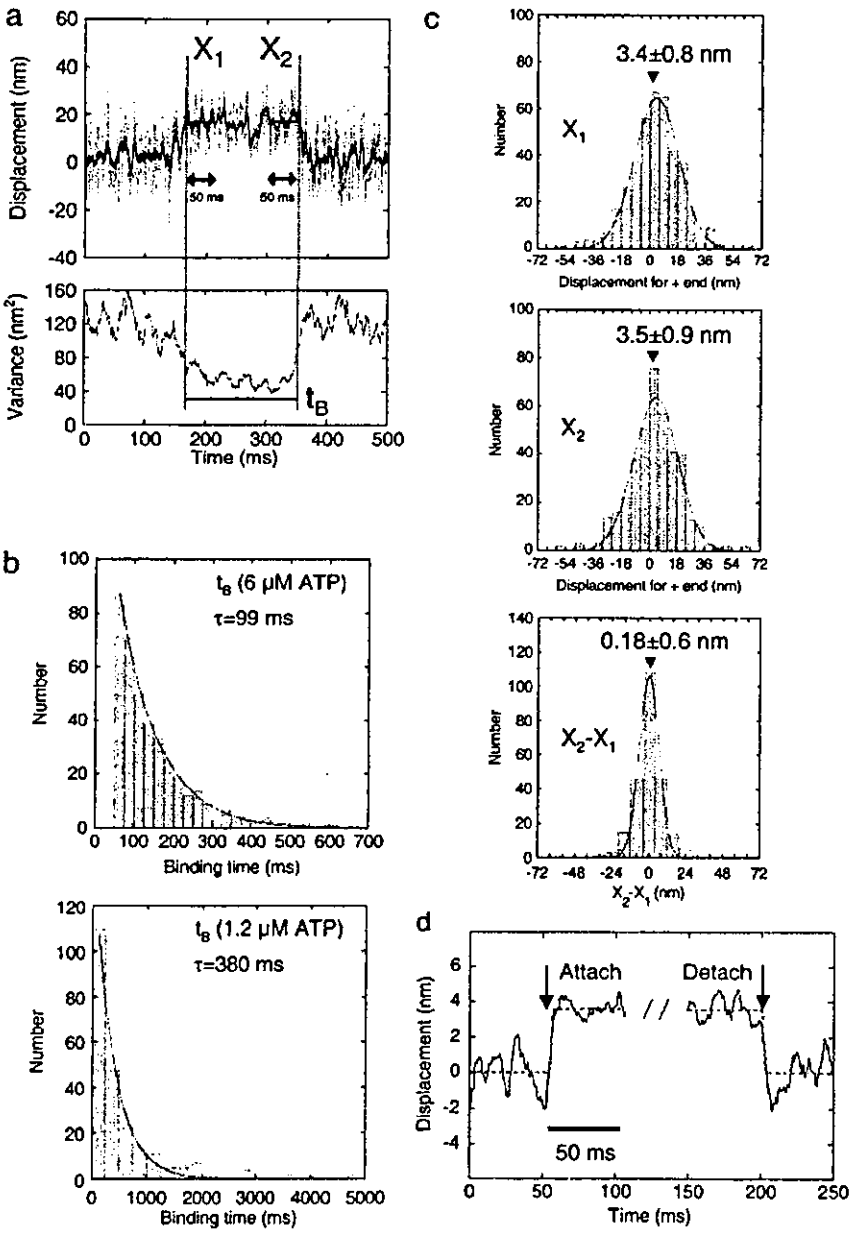

FIGURE 2 Analysis of the biased binding at 6 μM ATP. (*a*) The time course of the displacement and its variance of SHC-kinesin-beads are shown in the top and bottom panels, respectively. X_1 and X_2 indicate the average displacements from the trap center for 50 ms after binding and before dissociation. t_B is binding time from the initial binding to dissociation. (*b*) The histograms of the binding time in the presence of 6 μM ATP (*top*, n = 400) and 1.2 μM ATP (*bottom*, n = 245), respectively. (*c*) The histograms of X_1 (n = 400), X_2 (n = 400), and $X_1 - X_2$ (n = 242 for t_B > 100 ms) could be fitted to Gaussian curves with peaks at X_1 = 3.4 (mean ± SE = 0.8) nm, X_2 = 3.5 (mean ± SE = 0.9) nm, and $X_2 - X_1$ = 0.18 (mean ± SE = 0.6) nm. (*d*) Ensemble-averaged traces at binding and detachment by single molecules of SHC-kinesin. Each trace (through 200 Hz low pass filter) for 50 ms before and after the binding and detachment was fitted by rectangle curve represented as $d = a \times [1 + \exp\{-4(t - b)\}]^{-1} + c$, where d is displacement, t is time, a is the step size, and b and c are fitting parameters. Black solid curves are the ensemble traces synchronized at the binding and the detachment, and shaded dashed curves are rectangle curves with step displacement of 3.5 ~ 3.6 nm.

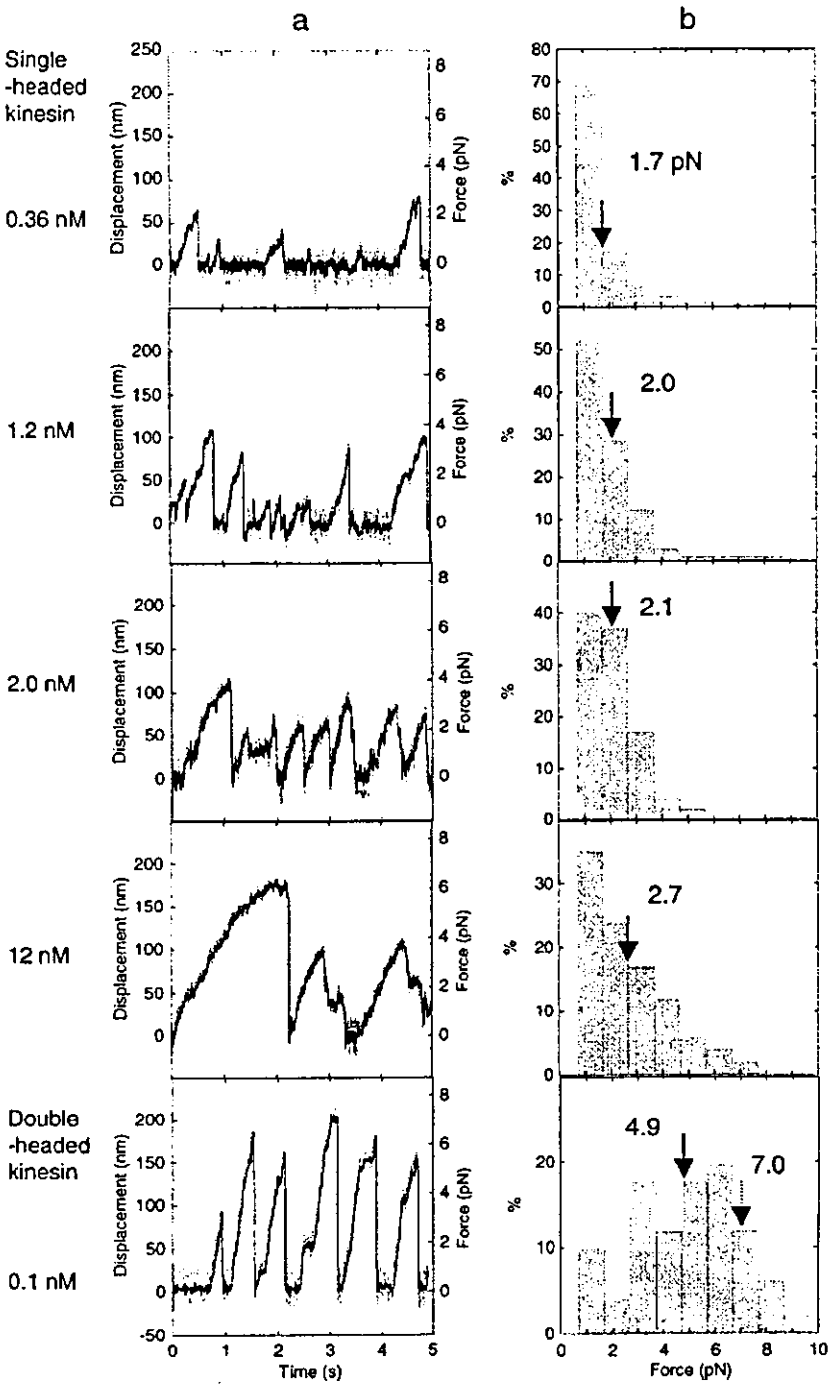

FIGURE 3 Force generation of the SHC-kinesin. (*a*) Force generation of SHC-kinesin at concentrations of 0.36, 1.2, 2.0, and 12 nM from top to bottom panels and that of single molecules of double-headed kinesin at concentration of 0.12 nM (*lowest panel*). (*b*) The histograms of the generated force of multiple molecules of SHC-kinesin and single molecules of double-headed kinesin. Solid arrows indicate the average forces, and broken arrow indicates the stall force.

The number of SHC-kinesin molecules bound to a bead was estimated using the Poisson distribution of the molecules on the bead. Single molecules of SHC-kinesin on a bead bound to and dissociated from a microtubule without undergoing processive movement. If single molecules of SHC-kinesin moved processively, the ratio of the beads moving continuously in the presence of ATP should be the same as that binding in the presence of AMP-PNP because single molecules of SHC-kinesin bind strongly to the microtubules in the presence of AMP-PNP. In this instance, the curve did not match the ratio of the beads moving continuously (Fig. 1 *e*, *dotted curve*, and *diamonds* and *circles*), indicating the lack of processive movement of single molecules of SHC-kinesin.

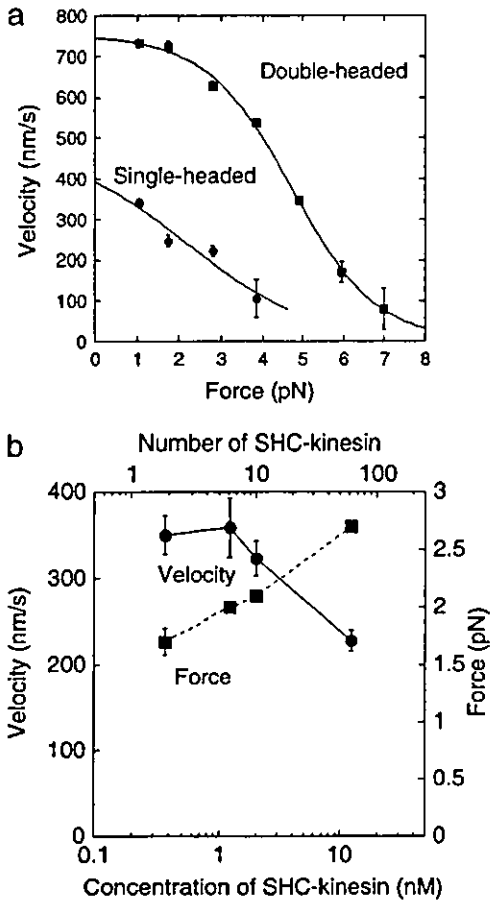

FIGURE 4 Movement of the SHC-kinesin. (*a*) Relationship between velocity and force of two SHC-kinesin molecules and single double-headed kinesin molecules are shown in circles ($n = 21$) and rectangles ($n = 15$), respectively. The curves could be well fitted to the equation, $V = 8/\{a + b \times \exp(kF)\}$, ($V$, velocity (nm/s); F, force (pN); a, b, and k are fitting parameters; Nishiyama et al., 2002). (*b*) Relationship between the number of SHC-kinesin molecules bound to a bead and velocity (*circles*) and force (*rectangles*), ($n = 87 \sim 100$ at each point).

In the in vitro motility assay, the run lengths of the microtubules moving on SHC-kinesins bound to the glass slides became shorter and even too short to detect when low concentrations of SHC-kinesin were used (Hancock and Howard, 1998; Young et al., 1998). This result indicates that the processivity of single molecules of SHC-kinesin is very low or nonexistent. However, the video analysis system had a limited spatial resolution of ~300 nm, thus the number of steps <38 (≈300 nm/8 nm) could not be counted (Hancock and Howard, 1998). In this study, only one step could be detected by using the optical tweezers apparatus with high spatial resolution. Steps longer than 8 nm in length, however, were not observed during the binding of SHC-kinesin to the microtubule. Using traces that had been averaged, there was no significant displacement from the binding to the dissociation of SHC-kinesin (0.18 ± 0.60 nm; Fig. 2 *c*). This result clearly indicates that single molecules of SHC-kinesin did not take any additional steps once they had bound to the microtubules. Thus, it appears that single molecules of SHC-kinesin bound to and dissociated from a microtubule upon the hydrolysis of ATP without undergoing any stepwise movement.

Biased binding and dissociation of SHC-kinesin

At low SHC-kinesin concentrations (<0.1 nM), beads were observed to bind to and then dissociate from a microtubule (Fig. 1 *b*) at low concentrations of ATP (Fig. 1 *e*, *triangles* and *diamonds*). At ATP concentrations of 6 and 1.2 μM, the time constants for binding were 99 and 380 ms, respectively. These values are in agreement with the cycle time of ATP hydrolysis by single molecules of SHC-kinesin which had been calculated using a kinetic parameter, K_m=43 μM ATP, to be 101 and 460 ms, respectively (Huang and Hackney, 1994). The histograms of the binding time showed an exponential decay (Fig. 2 *b*), indicating that the hydrolysis of single ATP molecules could be approximately described by a first order reaction. This kinetic analysis supported the observation that the binding and dissociation would be performed within a single turnover of ATP by single molecules of SHC-kinesin. The binding of SHC-kinesin to a microtubule in the presence of 1 mM ATP was not observed because the binding time was too brief to detect (12 ms, estimated from the ATPase rate at 1mM ATP).

SHC-kinesin binds to a microtubule when in the ADP binding state because ADP release is a rate limiting step in the absence of microtubules (Hackney, 1995). After ADP release, SHC-kinesin binds strongly to a microtubule in a nucleotide free state. The SHC-kinesin and microtubule complex then hydrolyze ATP into ADP·P_i. After P_i is released, the SHC-kinesin in the ADP binding state dissociates from the microtubule because, in this state, it has a low affinity to the microtubules (Hackney, 1995). Thus, the binding, hydrolysis, and detachment of SHC-kinesin to a microtubule can be described as follows:

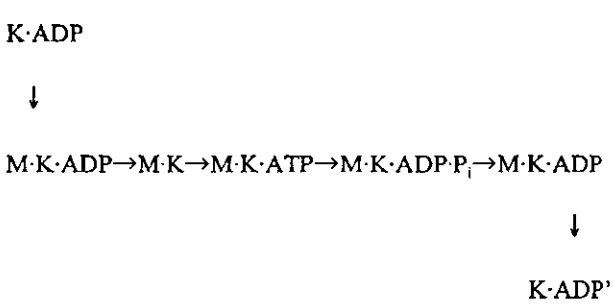

where M and K indicate a microtubule and an SHC-kinesin, respectively.

SHC-kinesin bound to a microtubule in the direction biased toward the plus end of 3.5 nm (Fig. 2 *c*). The 3.5-nm

biased displacement was generated at the time of binding or within 30 ms of binding to a microtubule (Fig. 2 *d*). Since the ATP free state was calculated to be ~100 ms at an ATP concentration of 6 μM from biochemical result (Huang and Hackney, 1994), the bias displacement occurred before the binding of ATP, that is, when it was bound to the microtubule or when ADP was released. The average 3.5 nm biased displacement was due to the translational movement of the SHC-kinesin head along a microtubule and an angular change of SHC-kinesin neck. Okada et al. (2003) evaluated the influence of the angular change of the neck linker of KIF1A by measuring the displacement of the beads bound to the N- and C-termini of KIF1A, respectively. The same relation between the steps and force of both the N- and C-termini indicates that the angular change of the neck linker did not affect the biased binding of KIF1A. The contribution of angular change will also be small on SHC-kinesin.

Continuous movement by multiple molecules of SHC-kinesin

The minimum number of SHC-kinesin molecules needed for continuous movement is two (Fig. 1 *e*). To move processively, it is essential that kinesin molecules have the directional displacement and do not dissociate from the microtubules. Directional movement by biased binding could be produced when two or more SHC-kinesin molecules attached to a bead. In this case, one molecule could produce the directional movement, whereas the other prevents the kinesin from dissociating from the microtubule (Tomishige et al., 2002). Inoue et al. (2001) observed the movement of single molecules of the fluorescently labeled SHC-kinesin with or without BCCP. They suggested that BCCP had some affinity for the microtubule preventing it from dissociating. In our experiment, it is possible that BCCP did not bind to the microtubule because the BCCP of SHC-kinesin at the C-termini was bound to a bead via streptavidin. As a result, the nonprocessive movement of single molecules of SHC-kinesin could be observed.

Both the velocity and force of two molecules of SHC-kinesin were lower than those of double-headed kinesin (Fig. 4 *a*). The reason for this reduction could be that the position and direction of SHC-kinesin binding to microtubules is not optimal because of the random binding to the beads. The probability that backward steps occurred (8–20 nm) was <6% for double-headed kinesin, and that increased to ~20% for SHC-kinesin with a 1–2 pN load (data not shown). This increment in the frequency of backward movement would also contribute to the slower velocity.

Inoue et al. (1997) reported that the velocity and force of multiple molecules of SHC-kinesin in the absence of BCCP was comparable to that of double-headed kinesin. It has been suggested that SHC-kinesin attached to a small molecule of biotin, ~0.5 nm in diameter, can bind to two sites on the single molecules of streptavidin, forming a pseudo-double-headed kinesin (Inoue et al., 1997). A BCCP of SHC-kinesin, ~3 nm in diameter, should sterically block another SHC-kinesin binding to neighboring binding sites on an avidin because the distance between binding sites was ~1 nm (Weber et al., 1989). Okada and colleagues suggested that the single-headed kinesin with BCCP on the avidin did not form a dimer because the F_{ab} fragment of the antibody with a single binding site to kinesin had similar binding and movement ratios to those of streptavidin (Okada et al., 2003). In this study, two molecules of SHC-kinesin bound randomly to a bead. This resulted in the production of low forces and beads that moved at a slow velocity because the heads were not able to interact with the microtubule in the optimum orientation.

The force and the sliding velocity remained almost constant when the average number of SHC-kinesin molecules on a bead was between 1 and 10 (Fig. 4 *b*). The number of molecules interacting simultaneously with the microtubule was calculated to be ~2 (occasionally 3) from the geometry of kinesin and the microtubules (Fig. 1 *e*, *solid* and *dashed curves*). Therefore, two molecules of SHC-kinesin produced a force of ~2 pN in average.

When ~60 molecules of SHC-kinesin were bound to a bead, the force increased and the velocity of sliding decreased (Fig. 4 *b*). The reason for the large forces is the number of molecules interacting simultaneously with a microtubule increases to >3. The decrease in velocity may be explained by an increase in the number of SHC-kinesin interacting with a microtubule in an unsuitable orientation and/or position. The slow velocity of the microtubules interacting with SHC-kinesin has also been observed in the motility assays by our lab (~120 nm/s, data not shown) and others (Hancock and Howard, 1998; Inoue et al., 2001; Young et al., 1998). This result suggests that SHC-kinesin molecules interact with the microtubules in a less than optimum orientation which may inhibit the motility.

Model of the unidirectional movement by SHC-kinesin

Single molecules of SHC-kinesin in the ADP binding state bind to tubulin with a displacement of x nm as a result of Brownian motion (Fig. 5 *a*). Then SHC-kinesin moves an average of ~4 nm toward the plus end of the microtubule as biased binding. The SHC-kinesin and microtubule complex binds an ATP molecule to be hydrolyzed, and then SHC-kinesin in the ADP state dissociates from the microtubule.

The movement of two molecules of SHC-kinesin begins with the state where the rear head binds to a microtubule. In contrast, the front head is in the ADP binding state and is positioned over the microtubule (Fig. 5 *b*). The front head attaches to the microtubule with displacement of x nm to the plus end. The displacements, x, of the heads are considered to be positive because of the neck linker docking to the head or structural changes that occur during ATP hydrolysis (Kikkawa

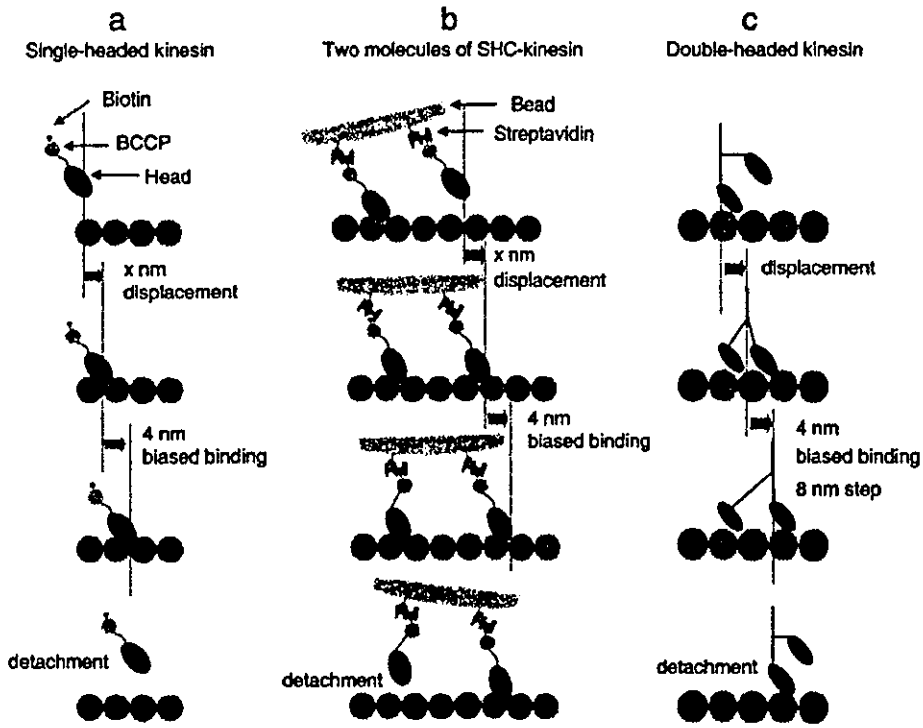

FIGURE 5 Movement models of SHC-kinesin and double-headed kinesin. (*a*) Single molecules of SHC-kinesin. (*b*) Two molecules of SHC-kinesin. (*c*) Single molecules of double-headed kinesin. Details are described in the text.

et al., 2001; Rice et al., 1999). The front head then releases ADP and binds strongly to the microtubule. At the same time, the ~4 nm biased displacement occurs to the plus end of the microtubule. Whereas the front head binds to a microtubule and produces force, the rear head is dissociated from the microtubule. The rear head then attaches to the microtubule with a displacement to the plus end as a result of the biased binding (data not shown). Finally, the front head dissociates from the microtubule once it is in the ADP binding state. Alternatively, the role of the front head could be exchanged with that of the rear head. Repetitions of these cycles generate the continuous movement. The regular 8 nm steps typically observed with double-headed kinesin were not observed for SHC-kinesin (data not shown). The distance between the heads and the SHC-kinesin interactions with the protofilaments most likely take steps of varying size but those other than 8 nm.

Double-headed kinesin motility begins with the state in which the front head with ADP attached is positioned over a microtubule and the rear head without nucleotides is bound to the microtubule (Hancock and Howard, 1999; Fig. 5 *c*). The front head attaches to a microtubule with a displacement toward the plus end of the microtubule. Either before or after the displacement, the single-head moves by ~4 nm toward the plus end as biased binding and completes the 8 nm step, suggesting the existence of substeps (Nishiyama et al., 2001). The rear head is pulled forward by the front head and then dissociates from the microtubule (Uemura and Ishiwata, 2003). Repetitions of these cycles generate the unidirectional processive movement of 8 nm by the hand-over-hand mechanism (Asbury et al., 2003; Crevel et al., 1999; Higuchi et al., 2004; Kaseda et al., 2003; Yildiz et al., 2004).

According to our model, two molecules of SHC-kinesin and single molecules of double-headed kinesin move through the biased binding of single molecules of SHC-kinesin. Therefore, 'bias binding' is the key mechanism for the movement of motor proteins.

APPENDIX

Model simulation for determining the minimum number of SHC-kinesin molecules required on a bead for continuous movement

The minimum number of SHC-kinesin molecules required for the continuous movement was determined using a model calculation, when n equals the number of molecules bound randomly on a bead, 200 nm in diameter. The probability, $q(n, m)$, of n molecules bound on a bead out of an average number of molecules (m) was represented by $m^n e^{-m}/n!$ according to a Poisson distribution. A bead is a sphere, and the length between the BCCP-biotin and the microtubule binding site is relatively short (<10 nm, considering the configurations of SHC-kinesin and BCCP; Rice et al., 1999; Vale and Milligan, 2000). Thus, there is a limited distance between SHC-kinesin molecules, so this will limit the number of molecules that can simultaneously interact with a microtubule.

If the minimum number of molecules is two, the distances between every two molecules among n molecules can be calculated and the minimum distance between molecules, d_{min}, determined. The number of beads where d_{min} was shorter than the threshold distance d_0 (nm) where two SHC-kinesin molecules were able to interact simultaneously with a microtubule were counted. The probabilities, $p_2(n, d_{min} < d_0)$, are given by the number of the beads ($d_{min} < d_0$) divided by the calculated number of beads (1000 trials at each n in this work). The total probability, $P_2(m) = \Sigma q(n, m) \cdot \times p_2(n, d_{min} <$

d_0), $n = 2$–∞. The best value of d_0 was obtained by fitting $P_2(m)$ to the experimental data to give a value of 48–62 nm ($R = 0.98$, 0.95 for $d_0 = 48$, 62 nm). From this d_0 value, the possible area where two SHC-kinesin molecules interact simultaneously with a microtubule was calculated to be 6%–10% of the total area of a bead. Thus, the minimum distance required for an SHC-kinesin to interact with a microtubule from the bead surface was calculated to be 3–5 nm. This is consistent with the result obtained for KIF1A (Okada et al., 2003).

The model simulation for the minimum number of three molecules is as follows. All combinations (${}_nC_3$ ways) of three molecules out of a total of n molecules were selected. The number of beads on which the selected three molecules interacted simultaneously with a microtubule was counted. The probability, $p_3(n, d_0, l_0)$, where d_0 (nm) is the threshold distance between SHC-kinesins and l_0 (nm) is the width of microtubule, was given by the number of beads counted divided by the total number of the calculated beads (1000 trials at each n, in this work). The total probability, $P_3(m)$, that three molecules interacted simultaneously with a microtubule is represented by $P_3(m) = \Sigma q(n) \times p_3(n, d_0, l_0)$, $n = 3$–∞. When $l_0 = 25$ nm (diameter of microtubules) and $d_0 < 48$–62 nm (the minimum distance for an SHC-kinesin to interact with a microtubule from the bead surface is 3–5 nm), $P_3(m)$ did not fit the experimental data. Even when $d_0 = 105$ nm where the distance between the microtubule and the bead surface is 15 nm, i.e., longer than the length of SHC-kinesin, the simulated curve did not fit to the experimental data. These results indicate that the minimum number of molecules required for the continuous movement is two but not three.

We thank Dr. N. Sasaki for helpful discussion and Dr. J. West for critically reading this manuscript. This work was supported by Grants-in-Aid for Scientific Research in Priority Areas from the Japan MEXT (H.H.).

REFERENCES

Asbury, C. L., A. N. Fehr, and S. M. Block. 2003. Kinesin moves by an asymmetric hand-over-hand mechanism. *Science*. 302:2130–2134.

Berliner, E., E. C. Young, K. Anderson, H. K. Mahtani, and J. Gelles. 1995. Failure of a single-headed kinesin to track parallel to microtubule protofilaments. *Nature*. 373:718–721.

Bloom, G. S., M. C. Wagner, K. K. Pfister, and S. T. Brady. 1988. Native structure and physical properties of bovine brain kinesin and identification of the ATP-binding subunit polypeptide. *Biochemistry*. 27:3409–3416.

Crevel, I., N. Carter, M. Schliwa, and R. Cross. 1999. Coupled chemical and mechanical reaction steps in a processive *Neurospora* kinesin. *EMBO J.* 18:5863–5872.

deCastro, M. J., R. M. Fondecave, L. A. Clark, C. F. Schmidt, and R. J. Stewart. 2000. Working strokes by single molecules of the kinesin-related microtubule motor ncd. *Nat. Cell Biol.* 2:724–729.

Endow, S. A., and H. Higuchi. 2000. A mutant of the motor protein kinesin that moves in both directions on microtubules. *Nature*. 406:913–916.

Hackney, D. D. 1995. Highly processive microtubule-stimulated ATP hydrolysis by dimeric kinesin head domains. *Nature*. 377:448–450.

Hancock, W. O., and J. Howard. 1998. Processivity of the motor protein kinesin requires two heads. *J. Cell Biol.* 140:1395–1405.

Hancock, W. O., and J. Howard. 1999. Kinesin's processivity results from mechanical and chemical coordination between the ATP hydrolysis cycles of the two motor domains. *Proc. Natl. Acad. Sci. USA*. 96:13147–13512.

Higuchi, H., C. E. Bronner, H. W. Park, and S. A. Endow. 2004. Rapid double 8-nm steps by a kinesin mutant. *EMBO J.* 23:2993–2999.

Howard, J. 2001. Mechanics of Motor Proteins and the Cytoskeleton. Sinauer Associates, Sunderland, MA.

Howard, J., A. J. Hudspeth, and R. D. Vale. 1989. Movement of microtubules by single kinesin molecules. *Nature*. 342:154–158.

Howard, J., and A. A. Hyman. 1993. Preparation of marked microtubules for the assay of the polarity of microtubule-based motors by fluorescence microscopy. *Methods Cell Biol.* 39:105–113.

Huang, T.-G., and D. D. Hackney. 1994. *Drosophila* kinesin minimal motor domain expressed in *Escherichia coli*. *J. Biol. Chem.* 269:16493–16501.

Inoue, Y., A. H. Iwane, T. Miyai, E. Muto, and T. Yanagida. 2001. Motility of one-headed kinesin molecules along microtubules. *Biophys. J.* 81: 2838–2850.

Inoue, Y., Y. Y. Toyoshima, A. H. Iwane, S. Morimoto, H. Higuchi, and T. Yanagida. 1997. Movements of truncated kinesin fragments with a short or an artificial flexible neck. *Proc. Natl. Acad. Sci. USA*. 94:7275–7280.

Iwatani, S., A. H. Iwane, H. Higuchi, Y. Ishii, and T. Yanagida. 1999. Mechanical and chemical properties of cysteine-modified kinesin molecules. *Biochemistry*. 38:10318–10323.

Kaseda, K., H. Higuchi, and K. Hirose. 2003. Alternate fast and slow stepping of a heterodimeric kinesin molecule. *Nat. Cell Biol.* 5:1079–1082.

Kikkawa, M., E. P. Sablin, Y. Okada, H. Yajima, R. J. Fletterick, and N. Hirokawa. 2001. Switch-based mechanism of kinesin motors. *Nature*. 411:439–445.

Kojima, H., E. Muto, H. Higuchi, and T. Yanagida. 1997. Mechanics of single kinesin molecules measured by optical trapping nanometry. *Biophys. J.* 73:2012–2022.

Kuznetsov, S. A., E. A. Vaisberg, N. A. Shanina, N. N. Magretova, Y. Y. Chernyak, and V. I. Gelfand. 1988. The quaternary structure of bovine brain kinesin. *EMBO J.* 7:353–356.

Nishiyama, M., H. Higuchi, and T. Yanagida. 2002. Chemomechanical coupling of the forward and backward steps of single kinesin molecules. *Nat. Cell Biol.* 4:790–797.

Nishiyama, M., E. Muto, Y. Inoue, T. Yanagida, and H. Higuchi. 2001. Substeps within the 8-nm step of the ATPase cycle of single kinesin molecules. *Nat. Cell Biol.* 3:425–428.

Okada, Y., H. Higuchi, and N. Hirokawa. 2003. Processivity of the single-headed kinesin KIF1A through biased binding to tubulin. *Nature*. 424: 574–577.

Okada, Y., and N. Hirokawa. 1999. A processive single-headed motor: kinesin superfamily protein KIF1A. *Science*. 283:1152–1157.

Okada, Y., and N. Hirokawa. 2000. Mechanism of the single-headed processivity: diffusional anchoring between the K-loop of kinesin and the C terminus of tubulin. *Proc. Natl. Acad. Sci. USA*. 97:640–645.

Rice, S., A. W. Lin, D. Safer, C. L. Hart, N. Naber, B. O. Carragher, S. M. Cain, E. Pechatnikova, E. M. Wilson-Kubalek, M. Whittaker, E. Pate, R. Cooke, and others. 1999. A structural change in the kinesin motor protein that drives motility. *Nature*. 402:778–784.

Svoboda, K., and S. M. Block. 1994. Force and velocity measured for single kinesin molecules. *Cell*. 77:773–784.

Svoboda, K., C. F. Schmidt, B. J. Schnapp, and S. M. Block. 1993. Direct observation of kinesin stepping by optical trapping interferometry. *Nature*. 365:721–727.

Tomishige, M., D. R. Klopfenstein, and R. D. Vale. 2002. Conversion of Unc104/KIF1A kinesin into a processive motor after dimerization. *Science*. 297:2263–2267.

Uemura, S., and S. Ishiwata. 2003. Loading direction regulates the affinity of ADP for kinesin. *Nat. Struct. Biol.* 10:308–311.

Vale, R. D., and R. A. Milligan. 2000. The way things move: looking under the hood of molecular motor proteins. *Science*. 288:88–95.

Veigel, C., L. M. Coluccio, J. J. Jontes, J. C. Sparrow, R. A. Milligan, and J. E. Molloy. 1999. The motor protein myosin-I produces its working stroke in two steps. *Nature*. 398:530–533.

Weber, P. C., D. H. Ohlendorf, J. Wendoloski, and F. R. Salemme. 1989. Structural origins of high-affinity biotin binding to streptavidin. *Science*. 243:85–88.

Yildiz, A., M. Tomishige, R. D. Vale, and P. R. Selvin. 2004. Kinesin walks hand-over-hand. *Science*. 303:676–678.

Young, E. C., H. K. Mahtani, and J. Gelles. 1998. One-headed kinesin derivatives move by a nonprocessive, low-duty ratio mechanism unlike that of two-headed kinesin. *Biochemistry*. 37:3467–3479.

nature
structural &
molecular biology

Mechanochemical coupling of two substeps in a single myosin V motor

Sotaro Uemura[1], Hideo Higuchi[2,3], Adrian O Olivares[4], Enrique M De La Cruz[4] & Shin'ichi Ishiwata[1,5]

Reprinted from nature structural & molecular biology, volume 11, september 2004

nature
structural &
molecular biology

Mechanochemical coupling of two substeps in a single myosin V motor

Sotaro Uemura[1], Hideo Higuchi[2,3], Adrian O Olivares[4], Enrique M De La Cruz[4] & Shin'ichi Ishiwata[1,5]

Myosin V is a double-headed processive molecular motor that moves along an actin filament by taking 36-nm steps. Using optical trapping nanometry with high spatiotemporal resolution, we discovered that there are two possible pathways for the 36-nm steps, one with 12- and 24-nm substeps, in this order, and the other without substeps. Based on the analyses of effects of ATP, ADP and 2,3-butanedione 2-monoxime (a reagent shown here to slow ADP release from actomyosin V) on the dwell time and the occurrence frequency of the main and the intermediate states, we propose that the 12-nm substep occurs after ATP binding to the bound trailing head and the 24-nm substep results from a mechanical step following the isomerization of an actomyosin-ADP state on the bound leading head. When the isomerization precedes the 12-nm substep, the 36-nm step occurs without substeps.

Myosin V belongs to the myosin superfamily of actin-based molecular motors and is involved in the intracellular transport of organelles[1–4]. Myosin V consists of two identical heavy chains, each composed of an N-terminal motor domain ('head'), a domain comprising six IQ motifs that bind light chains ('neck'), a coiled coil dimerization domain and a globular cargo-binding tail domain[1,3]. Myosin V is a processive motor that 'walks' along an actin filament toward the barbed end over a long distance without dissociating from the filament[5,6]. Electron microscopy of actomyosin V in the presence of low ATP concentrations shows both motor domains of myosin V bound to the actin filament at sites spaced 36 nm apart, which corresponds to the half pitch of the filament long-pitch helix[7]. Experiments using optical tweezers identified processive 36-nm steps of a bead, on which single myosin V molecules were adsorbed[6,8]. Moreover, it was shown that myosin V walks as a left-handed spiral motor along an actin filament, because the average step size is slightly shorter than the half pitch of the long-pitch actin helix[9].

The hand-over-hand walking model has received strong support from two recent experiments that (i) observed the orientation of the neck domain of myosin V by monitoring the polarization of a single fluorophore covalently attached to a light chain[10] and (ii) measured the stepwise displacement of a single fluorophore labeled at one of six light chains of myosin V[11].

Solution kinetic studies demonstrate that ADP release occurs at ~15 s^{-1} and limits the myosin V ATPase cycle[12]. Microscopic analysis of myosin V stepping under various nucleotide conditions is consistent with rate-limiting ADP release[13]. The next key target is to determine how the mechanical and biochemical cycles are coupled to each other at the single-molecule level.

Here, we focused on mechanical events and detected substeps that occur within each regular 36-nm step with high temporal resolution. Each regular 36-nm step is composed of two consecutive substeps, one generating a 12-nm substep and the other a 24-nm substep. To investigate how these substeps and the states attained after the steps are coupled to the ATPase cycle of myosin V, we examined the effects of ATP and ADP concentrations, and 2,3-butanedione 2-monoxime (BDM)[14]. We also examined the force dependence of the occurrence frequency of each step and substep, and the dwell time of each state.

RESULTS

Movement of myosin V along an actin filament

A single myosin V–coated bead was trapped with optical tweezers and brought into contact with a fluorescently labeled biotinylated actin filament, which was immobilized on an avidin-coated glass surface through biotinylated BSA (Fig. 1a). A focused red light (685 nm) laser was used to diagonally illuminate the bead, and its dark-field image was projected onto a quadrant photodiode. The bead displacement was determined by measuring the differential output of the quadrant photodiode with nanometer accuracy and a 10-kHz sampling rate[15]. The use of a 200-nm-diameter bead here instead of a 1-μm bead was essential to obtain a high spatiotemporal resolution.

An example of the time course of bead displacement along an actin filament (Fig. 1b) shows three consecutive runs of a single myosin V molecule along an actin filament at a saturating ATP concentration (1 mM). As the bead began to deviate from the trap center, a positive external load was applied to the myosin V–actin complex (toward the pointed end of an actin filament). Myosin V detached from actin at a stall force of ~3 pN. After detachment, the bead quickly returned to the

[1]Department of Physics, School of Science and Engineering, Waseda University, 3-4-1 Okubo, Shinjuku-ku, Tokyo 169-8555, Japan. [2]Department of Metallurgy, Graduate School of Engineering, [3]Center of Interdisciplinary Research, Tohoku University, Sendai, 980-8579, Japan. [4]Department of Molecular Biophysics and Biochemistry, Yale University, New Haven, Connecticut 06520, USA. [5]Advanced Research Institute for Science and Engineering, Waseda University, 3-4-1 Okubo, Shinjuku-ku, Tokyo 169-8555, Japan. Correspondence should be addressed to S.I. (ishiwata@waseda.jp).

Published online 1 August 2004; doi:10.1038/nsmb806

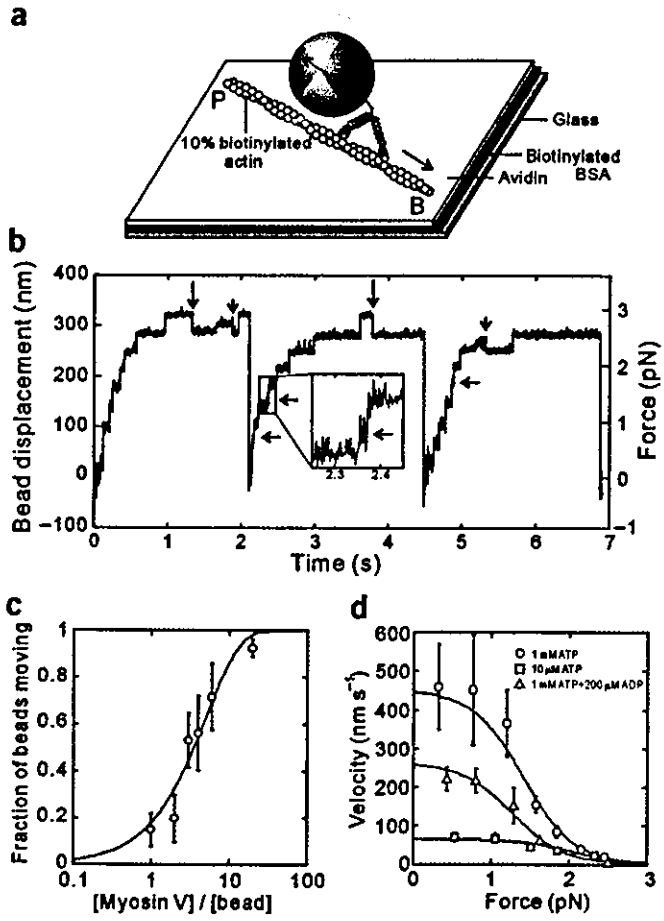

Figure 1 Stepwise movement of single myosin V motor under various external loads. (**a**) Schematic illustration showing how the movement of a myosin V–coated bead is measured. To allow the interaction of myosin V with an actin filament, the bead trapped with optical tweezers was moved onto a single actin filament attached to the glass surface through BSA using the biotin-avidin interaction. The position of the trap center was then fixed. The black and blue arrows, respectively, show the directions for the myosin V movement and the applied external load. (**b**) An example showing the displacement of the bead, where the consecutive 36-nm stepwise movements are clearly seen. A backward 36-nm step is shown by a large vertical arrow. A backward step for the substep is shown by a vertical small arrow. An intermediate state (shown by horizontal arrows) after a short step (substep) is sometimes observable; the 36-nm step in the middle trace is enlarged in an inset. The force was calculated from the displacement of the bead from the trap center times trap stiffness (0.009 pN nm^{-1} in b; right axis). (**c**) Relation between proportion of beads that moved along an actin filament and a mixing molar ratio of myosin V to beads. The proportion of moved beads (avg. ± s.d.) was obtained by examining three trials for each bead (20 different beads) at each point. A solid curve was obtained by fitting with $1 - e^{-\lambda C}$, where c is the mixing molar ratio of myosin V to beads, and λ (0.197) is the fitting parameter[9,17,18]. (**d**) Force-velocity relationship obtained under different conditions (n = 8–24 at each point, total = 405). The relationship shown by solid curves was obtained as described in the Methods section.

trap center and immediately began to deviate from the trap center again as a result of the processive motility of myosin V along actin.

We observed regular forward steps of ~36 nm, approximately equal to the half pitch of the actin filament helix. Nearly half of the 36-nm steps contained an 'intermediate state', indicated by horizontal arrows in Fig. 1b (compare inset). At higher forces ≥2 pN, backward 36-nm steps (see large vertical arrows in Fig. 1b) and backward steps from the intermediate state (see small vertical arrows in Fig. 1b) were identified[8,16].

To confirm that a single molecule is sufficient to generate the movement observed, we examined the fraction of beads that bind and move processively along an actin filament at various mixing ratios of myosin V and bead. We confirmed by statistical analysis that single myosin V molecules were sufficient to move the beads (Fig. 1c)[17,18].

The force-velocity relationships in the presence of 1 mM ATP (± ADP) were sigmoidal, showing a steep decrease in the velocity at higher than ~1 pN (Fig. 1d). In comparison, the relationship in the presence of 10 μM ATP showed a small force dependence. ADP release is rate limiting in the presence of 1 mM ATP[12], whereas ATP binding becomes rate limiting at low ATP concentrations[12]. The present results suggest that ADP release is more load dependent than ATP binding. It should be noted that the stall force, 2.5–3 pN, does not depend on the nucleotide conditions (Fig. 1d).

Measurement of substeps within each 36-nm step

The time course of bead movement examined on an expanded time scale with 0.1-ms time intervals clearly shows the existence of substeps within the regular 36-nm step (Fig. 2). We identified the presence of

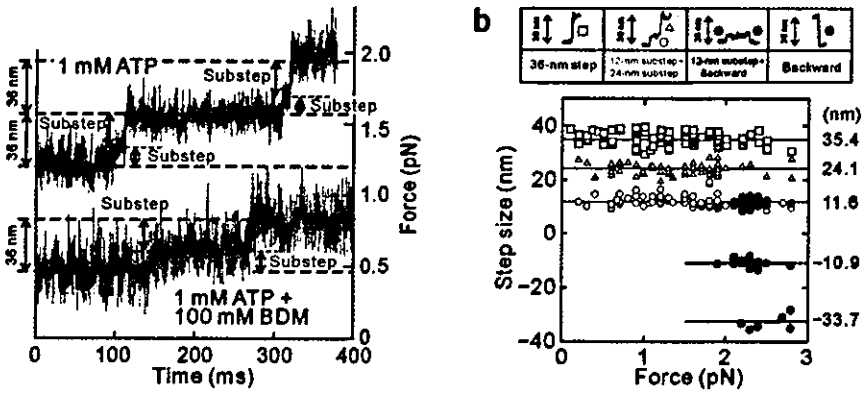

Figure 2 The time course of myosin V movement at a 10-kHz sampling rate and force dependence of the occurrence of various steps. (**a**) Consecutive two substeps at 1 mM ATP shown in the upper trace and at 1 mM ATP + 100 mM BDM shown in the lower trace. We determined whether or not substeps were present by obtaining the histogram of the bead positions at 0.1-ms time intervals (gray lines). Black lines were obtained by the smoothing of 21 successive points. (**b**) Force dependence of step size in the presence of 1 mM ATP. The size of the steps was estimated as described in Methods. The first 12-nm substep, blue circle; the second 24-nm substep, green triangle; the 36-nm step in which substeps could not be identified, red square; the 12-nm substep that was followed by a backward step, dark blue circle; the backward steps, black circles. We could not determine the occurrence of the 24-nm backward step. The figures along the right ordinate are the average step size estimated independent of force as shown by a straight line parallel to the abscissa.

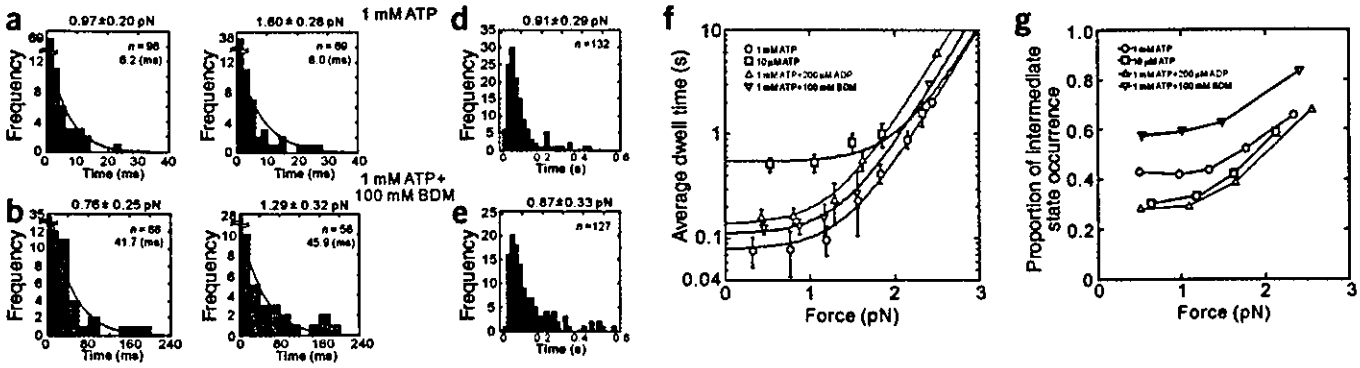

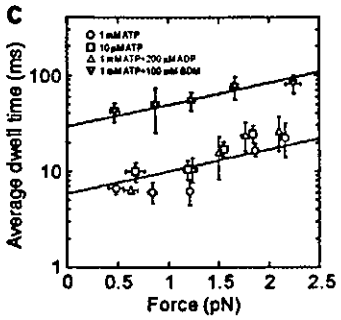

Figure 3 Force dependence of the intermediate and the main dwell times at various nucleotide states and of the occurrence frequency of the intermediate state. (**a**,**b**) Histogram showing the distribution of the dwell time, τ, of the intermediate state in the presence of 1 mM ATP in **a** and 1 mM ATP + 100 mM BDM in **b** at different force levels. The data <2 ms dwell time (pink bars in **a** and thin black bars in **b**) include those in which substeps could not be identified. The fitting curves (thin lines) expressed by $\exp(-\tau / \tau_0)$ were obtained without the data <2 ms (see text for explanation), where τ_0 is a time constant (equal to average dwell time) dependent on developed force. (**c**) Force dependence of the average dwell time, τ_0, of the intermediate state at 1 mM ATP, 10 μM ATP, 1 mM ATP + 200 μM ADP and 1 mM ATP + 100 mM BDM (n = 8–14 at each point, total = 225). The average dwell time was determined at several force levels different from those shown in **a** and **b**. Among the data shown in **a** and **b**, only the data in which the substeps were identified were used for the analysis in **c**. A red line was determined for the data at the first three conditions and a black line for the last condition by using a global fit analysis assuming the same slope for the two lines. (**d**,**e**) Histogram showing the distribution of the main dwell time, τ, in the presence of 1 mM ATP in **d** and 1 mM ATP + 100 mM BDM in **e** at low force level. (**f**) Force dependence of the average dwell time, τ_0 (= $k_1^{-1} + k_2^{-1}$) of the main state at 1 mM ATP, 10 μM ATP, 1 mM ATP + 200 μM ADP and 1 mM ATP + 100 mM BDM (n = 18–32 at each point, total = 562). The average dwell time was determined at several force levels different from those shown in **d** and **e**. All the data shown in **d** and **e** were used for the analysis in **f**. The force dependence of τ_0 for each condition was expressed by $\tau_0 \exp(Fd_0 / k_BT) + \tau_C$, where τ_C is the time constant representing the dwell time independent of force. The values obtained are summarized in **Table 1**. (**g**) The occurrence frequency of the intermediate state at several force levels for each nucleotide condition. Not only the 36-nm steps with substeps but also those without substeps are included in the first column shown by pink and thin black bars in **a** and **b**. Thus, the occurrence frequency of the 36-nm main steps without substeps was estimated by subtracting that obtained by extrapolating the exponential function of the dwell time distribution for the intermediate state.

the intermediate state by making a histogram of the bead position before and after each 36-nm step. We refer to each 36-nm step, in which substeps could not be identified, as a 'main step'. The state populated after the main step or subsequent to the intermediate state is termed a 'main state'. The intermediate state had a lifetime of a few milliseconds at low forces in the presence of 1 mM ATP (an upper trace in Fig. 2a) and tens of milliseconds in the presence of 100 mM BDM (lower trace in Fig. 2a). The main state had a longer lifetime (several tens of milliseconds) than the intermediate state in all the conditions tested. The substeps occurred at random and did not correlate with the occurrence of the 36-nm main steps.

The step size was determined directly from the time course of stepwise movements of the myosin V–coated bead. A step size distribution had peaks at 11.6 nm (12-nm substep), 24.1 nm (24-nm substep) and 35.4 nm (36-nm step in which substeps could not be identified), and included backward steps at 12 nm and 36 nm (Fig. 2b). The step size of either the two substeps or for the single main step depended little on the force level (Fig. 2b), although a possibility that the step size depends on the force level cannot be excluded because we did not take account of the attenuation factor to estimate the step size (see Methods). On the other hand, approaching the stall force, the occurrence frequency of 24-nm and 36-nm steps decreased and that of backward steps increased.

Characterization of the intermediate state

Histograms showing the distribution of intermediate state dwell times under several nucleotide and force conditions fit single exponentials regardless of the nucleotide conditions (Fig. 3a,b), indicating that this dwell time is coupled with a single chemical reaction. The decay time estimated by exponential fitting became longer as force (balanced to external load) increased. It should be noted here that the occurrence frequency <2 ms dwell time (shown by pink bars in Fig. 3a and thin black bars in Fig. 3b) largely exceeded that estimated from the exponential fitting of the dwell time, strongly suggesting that there is a pathway for the 36-nm main step without the intermediate state. In the Discussion, we attempt to construct a walking model that can explain this postulate.

The intermediate dwell time did not depend on the concentrations of ATP and ADP (Fig. 3c), suggesting that the intermediate state is not coupled with nucleotide binding or release. On the other hand, BDM markedly prolonged the intermediate dwell time (Figs. 2a and 3b).

The force dependence of the average dwell time of the intermediate state is expressed by the single exponential function of the force, $\tau_i \exp(Fd_i / k_BT)$, where τ_i is the average dwell time in the absence of force (F), d_i the characteristic distance (a parameter having the dimension of length that characterizes the bond instability against applied load), k_B the Boltzmann constant and T the absolute temperature (Fig. 3c). We determined the values of τ_i and d_i by global fitting of all the data[19,20], assuming that τ_i is only prolonged by the addition of BDM and d_i is common to all the conditions examined (see **Table 1**).

Characterization of the main state

In contrast to the intermediate dwell time (Fig. 3a–c), the histogram of the main dwell time (Fig. 3d,e) shows a peak. The main dwell time can be expressed by the sum of two exponential functions as shown previously[8], indicating that the main dwell time is coupled with two consecutive chemical reactions.

Table 1 Parameters obtained by dwell time analysis

	$\tau_{Total} = \tau_D \exp(Fd_D / k_BT) + \tau_C + \tau_i \exp(Fd_i / k_BT)$			
Nucleotide states	τ_{Total} ($F = 0$)	τ_D (ms), d_D (nm)	τ_C (ms)	τ_i(ms), d_i (nm)
1 mM ATP	86.7 ± 13.0	1.1 ± 0.3, 12.5 ± 0.4	79.7 ± 11.5	5.9 ± 1.2, 2.2 ± 0.2
1 mM ATP + 100 mM BDM	141.2 ± 16.2	1.7 ± 0.4, 12.5 ± 0.4	110.6 ± 9.2	28.9 ± 6.6, 2.2 ± 0.2
1 mM ATP + 200 μM ADP	145.5 ± 20.2	2.8 ± 0.3, 12.5 ± 0.4	136.8 ± 18.7	5.9 ± 1.2, 2.2 ± 0.2
10 μM ATP	553.5 ± 50.1	1.1 ± 0.3, 12.5 ± 0.4	546.5 ± 48.6	5.9 ± 1.2, 2.2 ± 0.2

The main dwell time was fit to the sum of a force-dependent exponential and a constant, whereas the intermediate dwell time was fit to a force-dependent single exponential. The values of parameters τ_D, d_D, τ_C, τ_i and d_i were determined by global fit with nonlinear optimization[19,20] using SigmaPlot 8.0. For the global fit analysis, we assumed that the values of d_D and d_i are common to the main and intermediate states, respectively, and τ_D and τ_i for some nucleotide states.

Either lowering the ATP concentration or adding ADP caused an increase in the average dwell time, τ_0 ($\tau_0 = k_1^{-1} + k_2^{-1}$) (Fig. 3f). This indicates that ATP binding and ADP release shorten the dwell time of the main state[8]. We also confirmed that the average dwell time increases with force (Fig. 3f). We observed that 100 mM BDM prolonged this dwell time at every force level.

The force (F) dependence of the average main dwell time is expressed by $\tau_D \exp(Fd_D / k_BT) + \tau_C$, where the values of τ_D, d_D and τ_C were determined by global fitting of all the data[19,20], assuming that d_D is common to all the conditions examined, τ_D is longer in the presence of either ADP or BDM, and τ_C is different at every condition. We conclude that τ_D is attributable to ADP release in the absence of load, because the value of τ_D is determined independent of the ATP concentration but prolonged by ADP and BDM (see Table 1). τ_C is a constant term, which increased on lowering the ATP concentration and adding ADP (see Table 1). Also, it is to be noted that the large value of d_D (12.5 nm) indicates that ADP release largely depends on the force level. (Note that this factor becomes predominant at the force level higher than ~1 pN in 1 mM ATP or ~2 pN in 10 μM ATP, as observed in Fig. 3f.)

Frequency of the intermediate state

The occurrence frequency of the intermediate state within the 36-nm main step is greatest in the presence of BDM and is increased with force irrespective of the nucleotide condition (Fig. 3g). In the absence of BDM, the proportion merged at a high force level irrespective of the nucleotide conditions, whereas at a low force level the proportion was decreased on lowering the ATP concentration and by the addition of ADP.

Effects of BDM on the ATPase kinetics of myosin V

Actin filaments activate the steady-state ATPase activity of MV-1IQ (Fig. 4a). The solid line in Fig. 4a is the best fit to a hyperbola (rate = (V_{max} × [actin] / (K_{ATPase} + [actin])). In the absence of BDM, the maximum turnover rate, V_{max}, was 13.7 ± 0.9 s^{-1} and the K_{ATPase} was 3.5 ± 0.6 μM, in agreement with earlier determinations[12,21,22]. BDM (100 mM) reduces the V_{max} and K_{ATPase} approximately two-fold to 6.9 ± 0.2 s^{-1} and 2.3 ± 0.2 μM, respectively. In agreement with an earlier study[23], ~10 mM BDM has no appreciable effect on the maximal steady-state cycling of MV-1IQ.

Actin filaments accelerate the rate of transient P_i release from MV-1IQ-ADP-P_i (Fig. 4b). Time courses of P_i release follow single exponentials (Fig. 4b inset) because myosin V is limited to a single ATP turnover by including excess ADP in the actin filament solution (see Methods). In the absence of BDM, the maximum rate of P_i release from MV-1IQ-ADP-P_i (k_{+4}' following nomenclature of ref. 24) was 60 ± 9 s^{-1} and the actin concentration at the half-maximum rate (K_9^{-1}, ref. 24) was 7.3 ± 0.6 μM. The rate of myosin V-ADP-P_i binding

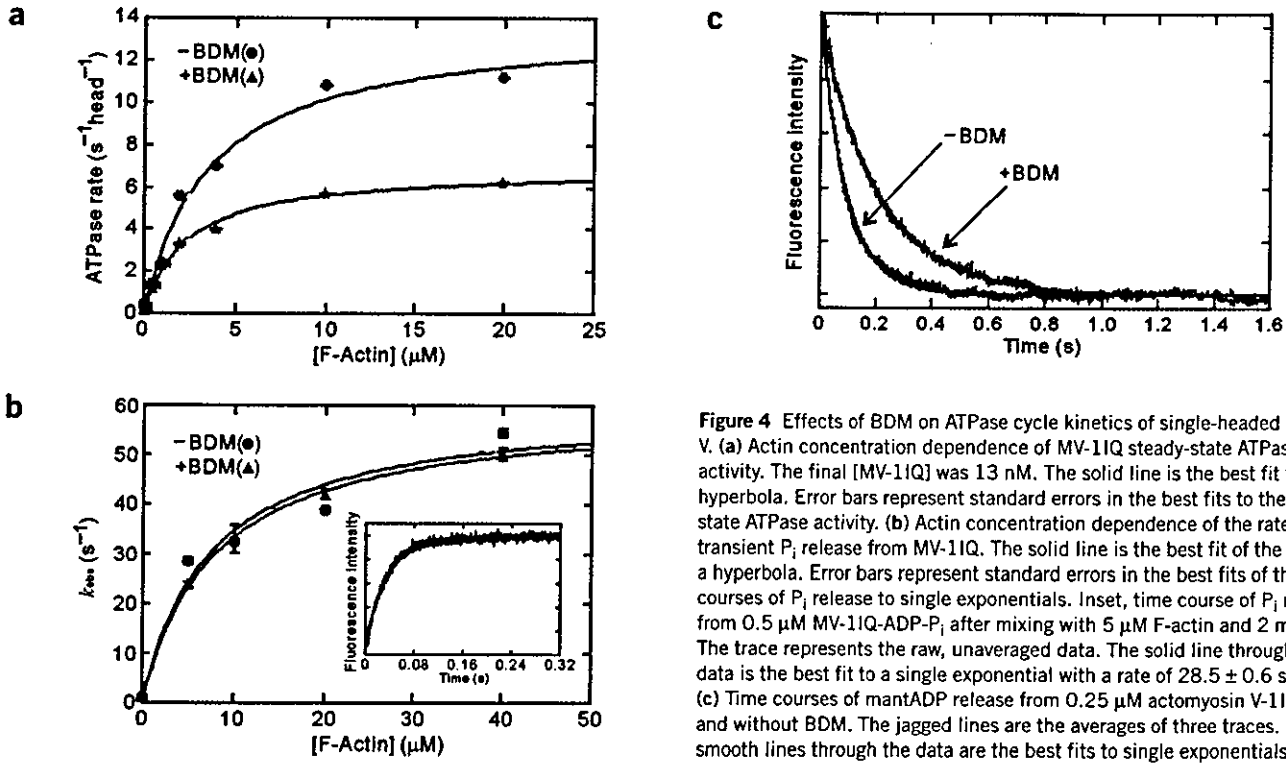

Figure 4 Effects of BDM on ATPase cycle kinetics of single-headed myosin V. (**a**) Actin concentration dependence of MV-1IQ steady-state ATPase activity. The final [MV-1IQ] was 13 nM. The solid line is the best fit to a hyperbola. Error bars represent standard errors in the best fits to the steady-state ATPase activity. (**b**) Actin concentration dependence of the rate of transient P_i release from MV-1IQ. The solid line is the best fit of the data to a hyperbola. Error bars represent standard errors in the best fits of the time courses of P_i release to single exponentials. Inset, time course of P_i release from 0.5 μM MV-1IQ-ADP-P_i after mixing with 5 μM F-actin and 2 mM ADP. The trace represents the raw, unaveraged data. The solid line through the data is the best fit to a single exponential with a rate of 28.5 ± 0.6 s^{-1}. (**c**) Time courses of mantADP release from 0.25 μM actomyosin V-1IQ with and without BDM. The jagged lines are the averages of three traces. The smooth lines through the data are the best fits to single exponentials.

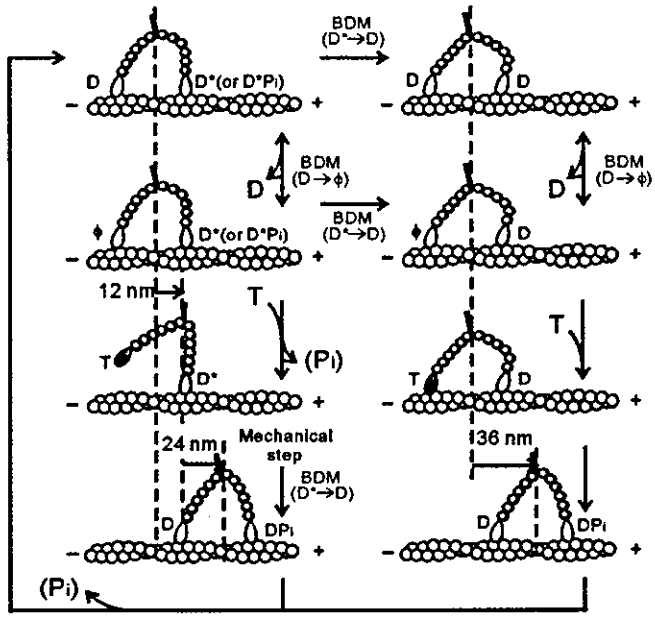

Figure 5 Hand-over-hand model coupled with nucleotide states explaining the present results. We propose that there are two possible pathways: pathway 1 in which 12-nm and 24-nm substeps occur (left column), and pathway 2 in which only the 36-nm main step occurs (right column). BDM is assumed to stabilize both the AMD complex (D) and the AM*D complex (D*), so that the transition rates indicated by red arrows are slowed down. T, ATP; D, ADP; P_i, inorganic phosphate; ϕ, no nucleotides; (P_i), a possible step at which P_i release occurs. For more details, see the text.

to actin filaments (K_9k_{+4}') was ~8 μM^{-1} s^{-1}, comparable to earlier measurements[12]. In the presence of 100 mM BDM, k_{+4}' was 59 ± 1.4 s^{-1} and K_9^{-1} was 7.7 ± 0.6 μM. BDM (100 mM) does not affect k_{+4}' or K_9^{-1} (Fig. 4b).

ADP release limits steady-state cycling of myosin V[12,21]. The rate of *N*-methylanthraniloyl-ADP (mantADP) release from actoMV-1IQ in the absence of BDM (Fig. 4c) was 10.2 ± 0.1 s^{-1}, in agreement with earlier determinations[12,21,22]. BDM (100 mM) slowed the rate of mantADP release approximately two-fold to 4.6 ± 0.1 s^{-1}. The reduction in ADP release accounts for the slower turnover rate in the presence of 100 mM BDM.

The K_{ATPase} of a myosin with rate-limiting ADP release ($k_{+5}' = V_{max}$) can be related to the maximum rate of P_i release (k_{+4}'), the actin concentration needed to reach half of the maximum P_i release rate (K_9, in units of M^{-1}), and the equilibrium constant for ATP hydrolysis (K_3)(ref. 21): $K_{ATPase} = k_{+5}'(K_9/k_{+4}')$ ($\{1 + K_3\}/K_3$). The two-fold reduction of ADP release (k_{+5}') by 100 mM BDM accounts for the two-fold reduction in V_{max} and K_{ATPase}, suggesting that BDM does not greatly affect the equilibrium constant for ATP hydrolysis (K_3), even though it was not measured directly. This result is in contrast to the case of muscle myosin II, where BDM stabilizes the actomyosin ADP-P_i state and accordingly suppresses P_i release[25]. Finally, we confirmed that the velocity of bead movement in the absence of external load decreased as the concentrations of BDM increased in the presence of 1 mM ATP. The BDM concentration dependence of the average bead velocity showed that the velocity decreases to nearly half with the addition of 100 mM BDM (data not shown). These results are consistent with those of the steady-state ATPase (Fig. 4a).

DISCUSSION

We propose here a hand-over-hand walking model of myosin V by taking into account all the experimental data described here together with those reported elsewhere[7,26,27].

First, considering that BDM reduces the rate of ADP release from actomyosin V (Fig. 4c) and largely prolongs the intermediate state (Fig. 3a–c), it is possible that the main species of the intermediate state is the actomyosin V–ADP complex and that the 24-nm substeps occur accompanied by the ADP release. However, this contradicts the observation that exogenous ADP does not affect the dwell time of the intermediate state. To resolve this apparent contradiction, we assume that isomerization exists in the actomyosin V (AM)–ADP complex, that is, AM*ADP (D*) and AMADP (D). It has already been proposed on the basis of a kinetic study using mant-nucleotides[13] that two states exist in the AM-ADP complex. Furthermore, it is well known that such an isomerization exists in the contraction mechanism of the muscle actomyosin II system[28]. Here, D is a complex produced by the binding of ADP to AM, whereas D* is produced after the hydrolysis of ATP on the AM-ATP complex[28,29]. We assume that D* is the major component of the intermediate state, implying that BDM stabilizes the D* state.

The intermediate state is terminated by the 24-nm substep, so that a straightforward deduction from such consideration is that the 24-nm substep occurs by the mechanical step mainly following the transition from D* to D (a part of the 24-nm substep may be attributable to the binding of detached head (T or DP_i) to actin after Brownian motion). It is notable that one set of researchers[30] showed that, in a single-headed myosin V, there exist two stable binding modes with different angles of the neck region in the ADP-bound state. Also, another group[31] recently showed that a one-headed myosin V produces a 25-nm working stroke.

The occurrence frequency of the 36-nm main step, in which the intermediate state could not be identified, was substantially larger than that predicted from the frequency extrapolated from the exponential fitting of the distribution of the dwell time of the intermediate states (Fig. 3a,b). This is understandable if we assume that there are two kinetic pathways for the 36-nm steps with (pathway 1) and without (pathway 2) passing through the intermediate state.

On the main state, the dwell time is largely prolonged on lowering the ATP concentration, and by adding ADP or 100 mM BDM (Fig. 3d–f), implying that it is shortened by the attachment of ATP and the detachment of ADP. The simplest assumption deduced from these results is that the main state is terminated; that is, the 12-nm substep occurs upon the ATP binding to a bound trailing head of myosin V from which ADP has been released. This assumption is similar to that predicted by Kolomeisky and Fisher[32] and also consistent with several models previously proposed for myosin V[7,22,24,26,27] and for myosin VI[24]. This is also consistent with the effect of BDM that slows the ADP release (Fig. 4c) and the overall ATPase activity as shown by the decrease in the velocity of myosin V movement (data not shown). That is, BDM stabilizes not only the D* state but also the D state.

Thus, we propose the hand-over-hand model as illustrated in Fig. 5, which incorporates the previous models[7,26,27] and which can explain, at least qualitatively, all the data presented here. First, the model can account for the existence of two kinds of steps: the 36-nm step composed of the sequential 12-nm and 24-nm substeps (pathway 1), and the 36-nm main step without substeps (pathway 2). The occurrence frequency of these two pathways depends on the conditions as discussed later. According to this model, the intermediate state is in a single-headed binding, whereas the main state is in a double-headed binding. This may be experimentally confirmed by the measurements of the stiffness of the protein-bead complex. In this respect, it is notable

that Veigel *et al.*[31] reported that the low stiffness intervals, which may imply the single-headed binding, exist during the main steps.

Second, the 12-nm substep is assumed to occur upon the binding of ATP to the bound trailing head. Although we do not know whether the bound leading head is D* or D*P_i at this stage (the upper left in Fig. 5), we infer that the 12-nm step may be attributable to the conformational change of the leading head due to the transition from DP_i to D* (or D*P_i).

Third, if the transition rate from D* to D decreases on increasing the force level, not only the dwell time of the intermediate state but also that of the main state are prolonged. Besides, we can understand that the higher the force level, the higher the occurrence frequency of the intermediate state irrespective of the nucleotide conditions (Fig. 3g), because the transition probability of the process shown by the horizontal arrows in Fig. 5 (from the pathway 1 to the pathway 2) is suppressed irrespective of the nucleotide conditions.

Fourth, because we assumed that BDM stabilizes not only the D* state but also the D state, both the intermediate state and the main state are stabilized, so that the dwell times of both states are expected to be prolonged. This assumption can also explain a large degree of extension of the dwell time, τ_i, of the intermediate state, because it is tightly coupled to the lifetime of the D* state, whereas the degree of extension of the dwell time of the main state was less because several other states must be involved in the main state.

Fifth, at low ATP concentrations, the attachment of ATP to the bound trailing head is slowed down, so that the probability increases that the transition from D* to D occurs at the bound leading head before ATP binds to the trailing head. This results in the increase in the occurrence frequency of the pathway 2. In the pathway 2, it is expected that the internal strain is largest within the D-D complex, because the leading head is considered to take the orientation similar to that realized after the 24-nm mechanical step. Thus, the D-D (also ϕ-D) complex may have a telemark shape as observed by electron microscopy[7]. It is to be stressed that the two pathways are not independent of each other, but the pathway 1 (or 2) is chosen when the transition from D* to D occurs after (or before) the 12-nm substep; that is, the model in Fig. 5 proposes that the timing of the 12-nm substep and the isomerization (the transition from D* to D) determines the pathways.

Finally, if the binding affinity of ADP for the bound trailing head is lower than that for the bound leading head because of the mechanochemical coupling due to the internal strain, ADP tends to detach from the bound trailing head, which results in the binding of ATP to the trailing head. Such an asymmetrical binding affinity of ADP may be prerequisite for the directional movement of myosin V toward the barbed end of an actin filament, although this must be experimentally confirmed. We infer that the loading-direction dependency of binding affinity of ADP assumed for myosin V is the reverse of that for kinesin as recently reported by us[20]. Also, another study[33] showed that the binding of ATP to the bound leading head is prerequisite for the directional movement of kinesin toward the plus-end of a microtubule. The correspondence between internal strain and nucleotide affinity in mechanochemical coupling for myosin V may be different from that for kinesin.

METHODS

Protein and assays used for optical trapping measurements. Myosin V was purified from chick brains[34]. Actin purified from rabbit skeletal muscle was biotinylated by 10% and, after polymerization, the filaments were labeled with rhodamine phalloidin (Molecular Probes)[35]. About 1 nM of fluorescent polystyrene beads (200 nm in diameter, yellow-green; Molecular Probes) were incubated for 20 min in an assay buffer (10 mM imidazole-HCl, pH 7.2, 75 mM KCl, 2.5 mM $MgCl_2$, 2 mM DTT and 0.1 mM EGTA) containing 10 mg ml^{-1} BSA. Myosin V (650 kDa) molecules were mixed with the beads at a molar ratio of 3:1 in assay buffer containing 300 mM KCl instead of 75 mM KCl as had been used in the previous studies. The average number of functional myosin V molecules on a bead was estimated by statistical analyses to be one (considering the geometry of the myosin V on the bead, we estimate that only single myosin V molecules interacted with an actin filament in almost all the measurements[17,20]). Assay buffer containing biotinylated BSA at 3 mg ml^{-1} was introduced into a flow cell and incubated for 2 min to coat the glass surface with biotinylated BSA. After rinsing with two volumes of assay buffer, 2 mg ml^{-1} streptavidin in assay buffer was flowed into the cell and incubated for 2 min. After rinsing with assay buffer, a solution of actin filaments, of which 10% was biotinylated and labeled with rhodamine-phalloidin, was flowed into the cell to allow binding of the filaments to the glass surface through avidin-bound biotinylated BSA. The flow cell was then filled with assay solution containing the myosin V–coated beads, filtered BSA and an oxygen-scavenging enzyme system[9]. The final solvent condition was approximately 0.1 pM myosin V–coated beads, 10 mM imidazole-HCl, pH 7.2, 75 mM KCl, 2.5 mM $MgCl_2$, 2 mM DTT, 0.1 mM EGTA, 3.6 mg ml^{-1} glucose, 0.08 mg ml^{-1} glucose oxidase, 0.01 mg ml^{-1} catalase, 0.95% (v/v) β-mercaptoethanol and nucleotides (1 mM ATP, 10 μM ATP, 1 mM ATP + 200 μM ADP or 1 mM ATP + 100 mM BDM). We were able to observe repeatedly the stepwise movements of myosin V–coated beads along the same actin filaments on the same beads, presumably for the same myosin V molecules, by using optical tweezers to manipulate the beads. All experiments on microscopy were done at 24 ± 1 °C.

We found that the percentage of biotinylation of actin is important for the processive movement of myosin V. In other words, myosin V could move processively on 1% and 10% biotinylated actin filaments, whereas it could not on 100% biotinylated ones, suggesting that the manner in which actin filaments bind to the glass surface is crucial. It should be noted that myosin V is reported to be a left-handed spiral motor[9], so that the revolution of a myosin V–coated bead around the actin filament could be sterically hindered. However, this possibility could be ignored, because the maximum distance of bead displacement was less than ~0.3 μm (Fig. 1b), such that it was much shorter than the distance, 2 μm, for one revolution[9].

The velocity of myosin V under no external load was obtained from the time course of bead movement along an actin filament in the absence of optical trap. The bead position was determined by the center of the fluorescence intensity distribution of the bead every video frame.

Proteins and reagents used for biochemical experiments. Actin was purified from rabbit skeletal muscle and gel filtered over Sephacryl S-300HR (ref. 12). The motor domain of myosin V containing the first IQ motif (MV-1IQ) and the essential light chain, LC-1sa, were co-expressed in Sf9 insect cells and purified by FLAG affinity chromatography[12]. The fluorescently labeled mutant of the phosphate-binding protein (MDCC-PBP; clone provided by M.R. Webb, National Institute for Medical Research, London) was expressed, purified and labeled as described[36]. ATP and ADP were purchased from Roche Molecular Biochemicals. mantADP was synthesized as described[37] or purchased from Molecular Probes with identical results. A molar equivalent of $MgCl_2$ was added to nucleotides immediately before use. BDM was purchased from Sigma (lot 092K1722) and prepared as a 250 mM stock solution in KMg50-MOPS (10 mM MOPS, pH 7.0, 50 mM KCl, 1 mM $MgCl_2$, 1 mM EGTA and 1 mM DTT) immediately before use[21].

Instrumentation and calibration. The myosin V–coated bead was trapped with an optical tweezers—that is, a focused infrared laser beam (λ = 1,064 nm, 2 W; Spectra Physics)—and illuminated diagonally by a focused red laser beam (λ = 685 nm, 20 mW; Phototechnica) through an objective lens (fluor ×100/1.3 oil; Nikon). The light scattered by the bead was gathered by an objective lens with an aperture (NA = 0.5, ×100 oil; Olympus) and projected onto a quadrant photodiode sensor (S4349; Hamamatsu Photonics) coupled to a differential amplifier (20-kHz roll-off frequency; OP711, Sentec). The fluorescently labeled beads and actin labeled with rhodamine-phalloidin were excited by a green laser (λ = 532 nm, 50 mW; Peace Engineering), and the fluorescence images were captured by a silicon-intensified target camera (C-2740; Hamamatsu Photonics) and displayed on a video monitor. The bead positions were

recorded on a computer equipped with a laboratory interface board (MacLab; AD Instruments)[15] at a sampling rate of 10 kHz through a digital low-pass filter at 10 kHz. The bead displacement was calibrated by moving the photodiode[15]. The trap stiffness of the optical tweezers was calibrated for every bead from the standard deviation of the position fluctuation of the trapped bead (0.009–0.011 pN nm^{-1}). The step size was obtained directly from individual stepwise movements of the bead at a sampling time of 0.1 ms and estimated as the difference between the average bead positions determined for 5 ms each interval just before and after the steps. We did not take into account the attenuation factor, which is a function of the stiffness of optical trap and the stiffness of the protein-bead complex[15,17], because the trap stiffness we used is considered to be much smaller than that of the protein-bead complex. The average velocity of bead movement (v) was estimated by dividing the average step size (36 nm) by the average total dwell time (τ_{Total} in units of ms) at each external load, which is balanced to the force (F) generated by myosin V. Force-velocity relationships were described by the following function: $v = 36\ nm / \tau_{Total} = 36/\{\tau_D \exp(Fd_D / k_BT) + \tau_C + \tau_i \exp(Fd_i / k_BT)\}$ (nm ms^{-1}), where τ_D, d_D, τ_C, τ_i, d_i, k_B and T are described in the text.

Steady-state and transient kinetic experiments. All kinetic experiments were done at 25 ± 0.1 °C in KMg50-MOPS with an SX.18MV-R stopped-flow apparatus (Applied Photophysics). Fitting was done with Pro-K software provided with the instrument. Steady-state ATPase activity of MV-1IQ was measured using the ATP-regenerating, NADH-coupled assay as described[21]. BDM had minimal effects on the assay components as determined by direct mixing with MgADP.

Transient P_i release of MV-1IQ was measured using MDCC-PBP (λ_{ex} = 430 nm, 455 nm emission filter) with the instrument in sequential mixing mode as described[24]. Briefly, 2 μM MV-1IQ (treated with 0.01 U ml^{-1} potato grade VII apyrase to remove residual ADP and ATP, ± 200 mM BDM) was mixed with 300 μM MgATP (± 200 mM BDM) and aged for 40–60 ms to allow for nucleotide binding and hydrolysis to occur, then mixed with an equal volume of a range of actin filament concentrations. As first described for myosin VI[24], myosin V was limited to a single ATP turnover by including 2 mM MgADP with the actin. ADP competes with ATP for binding to myosin V after the first turnover and inhibits subsequent steady-state cycling. Therefore, time courses follow single exponentials (see Fig. 4b inset) rather than exponentials followed by a linear steady-state component, permitting more accurate fitting of the P_i release time courses. This method of measuring P_i release can be used for all high-duty-ratio myosins with rapid rates of ADP binding and high ADP affinities.

ADP release was measured with a fluorescent nucleotide mantADP[12]. The fluorescence of mantADP (λ_{ex} = 366 nm, 400-nm emission filter) was monitored after an equilibrated mixture of 0.5 μM actomyosin V-1IQ (± 200 mM BDM) and 20 μM mantADP was mixed with an equal volume of 2 mM MgADP.

ACKNOWLEDGMENTS

We thank M.R. Webb for the phosphate-binding protein clone and suggestions on purification and labeling, and H.L. Sweeney for providing the myosin V heavy and light chain viruses. We are grateful to N. Sasaki, M.Y. Ali, K. Kinosita, Jr. and E.M. Ostap for encouragement and stimulating discussions. This research was partly supported by Grants-in-Aid for Specially Promoted Research, for the Bio-venture Project and for The 21st Century COE Program (Physics of Self-Organization Systems) at Waseda Univ. from the Ministry of Education, Sports, Culture, Science and Technology of Japan (to S.I.) and supported by a Scientist Development Grant from the American Heart Association and a grant from the US National Science Foundation (to E.M.D.L.C.). S.U. is a postdoctoral fellow of the Japan Society for the Promotion of Science. A.O.O. is supported by a Cellular & Molecular Biology graduate training grant (Yale University).

COMPETING INTERESTS STATEMENT

The authors declare that they have no competing financial interests.

Received 31 March; accepted 18 June 2004
Published online at http://www.nature.com/nsmb/

1. Cheney, R.E. *et al.* Brain myosin V is a two-headed unconventional myosin with motor activity. *Cell* **75**, 13–23 (1993).
2. Miller, K.E. & Sheetz, M.P. Characterization of myosin V binding to brain vesicles. *J. Biol. Chem.* **275**, 2598–2606 (2000).
3. Vale, R.D. The molecular motor toolbox for intracellular transport. *Cell* **112**, 467–480 (2003).
4. Reck-Peterson, S., Provance, D.W., Mooseker, M.S. & Mercer, J.A. Review: class V myosins. *Biochim. Biophys. Acta* **1496**, 36–51 (2000).
5. Sakamoto, T., Amitani, I., Yokota, E. & Ando, T. Direct observation of processive movement by individual myosin V molecules. *Biochem. Biophys. Res. Commun.* **272**, 586–590 (2000).
6. Mehta, A.D. *et al.* Myosin V is a processive actin-based motor. *Nature* **400**, 590–593 (1999).
7. Walker, M. *et al.* Two-headed bindings of a processive myosin to F-actin. *Nature* **405**, 804–807 (2000).
8. Rief, M. *et al.* Myosin V stepping kinetics: a molecular model for processivity. *Proc. Natl. Acad. Sci. USA* **97**, 9482–9486 (2002).
9. Ali, M.Y. *et al.* Myosin V is a left-handed spiral motor on the right-handed actin helix. *Nat. Struct. Biol.* **9**, 464–467 (2002).
10. Forkey, J.N., Quinlan, M.E., Shaw, M.A., Corrie, J.E. & Goldman, Y.E. Three-dimensional structural dynamics of myosin V by single-molecule fluorescence polarization. *Nature* **422**, 399–404 (2003).
11. Yildiz, A. *et al.* Myosin V walks hand-over-hand: single fluorophore imaging with 1.5-nm localization. *Science* **300**, 2061–2065 (2003).
12. De La Cruz, E.M., Wells, A.L., Rosenfeld, S.S., Ostap, E.M. & Sweeney, H.L. The kinetic mechanism of myosin V. *Proc. Natl. Acad. Sci. USA* **96**, 13726–13731 (1999).
13. Trybus, K.M., Krementsova, E. & Freyzon, Y. Kinetic characterization of a monomeric unconventional myosin V construct. *J. Biol. Chem.* **274**, 27448–27456 (1999).
14. Higuchi, H. & Takemori, S. Butanedione monoxime suppresses contraction and ATPase activity of rabbit skeletal muscle. *J. Biochem.* **105**, 638–643 (1989).
15. Nishiyama, M., Higuchi, H. & Yanagida, T. Chemomechanical coupling of the forward and backward steps of single kinesin molecules. *Nat. Cell Biol.* **4**, 790–797 (2002).
16. Moore, J.R., Krementsova, E.B., Trybus, K.M. & Warshaw, D.M. Myosin V exhibits a high duty cycle and large unitary displacement. *J. Cell Biol.* **155**, 625–635 (2001).
17. Kojima, H., Muto, E., Higuchi, H. & Yanagida, T. Mechanics of single kinesin molecules measured by optical trapping nanometry. *Biophys. J.* **73**, 2012–2022 (1997).
18. Svoboda, K., Schmidt, C.F., Schnapp, B.J. & Block, S.M. Direct observation of kinesin stepping by optical trapping interferometry. *Nature* **365**, 721–727 (1993).
19. Schnitzer, M.J., Visscher, K. & Block, S.M. Force production by single kinesin motors. *Nat. Cell Biol.* **2**, 718–723 (2000).
20. Uemura, S. & Ishiwata, S. Loading direction regulates the affinity of ADP for kinesin. *Nat. Struct. Biol.* **10**, 308–311 (2003).
21. De La Cruz, E.M., Sweeney, H.L. & Ostap, E.M. ADP inhibition of myosin V ATPase activity. *Biophys. J.* **79**, 1524–1529 (2000).
22. De La Cruz, E.M., Wells, A.L., Sweeney, H.L. & Ostap, E.M. Actin and light chain isoform dependence of myosin V kinetics. *Biochemistry* **39**, 14196–14202 (2000).
23. Ostap, E.M. 2,3-Butanedione monoxime (BDM) as a myosin inhibitor. *J. Muscle Res. Cell Motil.* **23**, 305–308 (2002).
24. De La Cruz, E.M., Ostap, E.M. & Sweeney, H.L. Kinetic mechanism and regulation of myosin VI. *J. Biol. Chem.* **276**, 32373–32381 (2001).
25. Herrmann, C., Wray, J., Travers, F. & Barman, T. Effect of 2,3-butanedione monoxime on myosin and myofibrillar ATPases. An example of an uncompetitive inhibitor. *Biochemistry* **31**, 12227–12232 (1992).
26. Spudich, J.A. & Rock, R.S. A crossbridge too far. *Nat. Cell Biol.* **4**, E8–E10 (2002).
27. Vale, R.D. Myosin V motor proteins: marching stepwise towards a mechanism. *J. Cell Biol.* **163**, 445–450 (2003).
28. Goldman, Y.E. and Brenner, B. Special topic: molecular mechanism of muscle contraction. *Annu. Rev. Physiol.* **49**, 629–636 (1987).
29. Dantzig, J.A., Hibberd, M.G., Trentham, D.R. & Goldman, Y.E. Cross-bridge kinetics in the presence of MgADP investigated by photolysis of caged ATP in rabbit psoas muscle fibres. *J. Physiol.* **432**, 639–680 (1991).
30. Burgess, S. *et al.* The prepower stroke conformation of myosin V. *J. Cell Biol.* **159**, 983–991 (2002).
31. Veigel, C., Wang, F., Bartoo, M.L., Sellers, J.R. & Molloy, J.E. The gated gait of the processive molecular motor myosin V. *Nat. Cell Biol.* **4**, 59–65 (2002).
32. Kolomeisky, A.B. & Fisher, M.E. A simple model describes the processivity of Myosin V. *Biophys. J.* **84**, 1642–1650 (2003).
33. Rosenfeld, S.S., Fordyce, P.M., Jefferson, G.M., King, P.H. & Block, S.M. Stepping and stretching. How kinesin uses internal strain to walk processively. *J. Biol. Chem.* **278**, 18550–18556 (2003).
34. Cheney, R.E. Purification and assay of myosin V. *Methods Enzymol.* **293**, 3–18 (1998).
35. Yanagida, T., Nakase, M., Nishiyama, K. & Oosawa, F. Direct observation of motion of single F-actin filaments in the presence of myosin. *Nature* **307**, 58–60 (1984).
36. Brune, M. *et al.* Mechanism of inorganic phosphate interaction with phosphate binding protein from *Escherichia coli*. *Biochemistry* **37**, 10370–10380 (1998).
37. Hiratsuka, T. New ribose-modified fluorescent analogs of adenine and guanine nucleotides available as substrates for various enzymes. *Biochim. Biophys. Acta* **742**, 496–508 (1983).

Pathological Evaluation of Sentinel Lymph Nodes for Breast Cancer

Takuya Moriya,[1] Shin Usami,[1,2] Hiroshi Tada,[2] Atsuko Kasajima,[1] Kazuyuki Ishida,[1,2] Yoshiyuki Kariya,[1] Noriaki Ohuchi[2] and Hironobu Sasano,[1] Departments of [1]Pathology and [2]Surgery, Tohoku University Hospital, Sendai, Japan.

Recently, sentinel lymph node (SLN) biopsy has been employed to avoid unnecessary lymph node dissection, because SLN negativity for carcinoma metastases may imply an extremely low possibility of non-SLN involvement. Pathological evaluation is essential, but standardized procedures have not yet been determined. Intraoperative consultation, either by frozen section (multiple slices are desirable) or touch imprint cytology, are usually very useful. Their accuracy, however, is variable and depends on the procedures used, but specificity is characteristically 100%, and the missed metastatic focus is always quite minute. After fixation, multiple sections, immunohistochemistry, and their combination will be able to detect small metastatic foci more frequently. The clinical significance of small or submicro- or occult metastases have not yet been clarified, and further investigations are needed. If the SLN is positive for carcinoma metastases, both the procedure for detection and the size of the metastatic focus should be clarified on the pathological reports. [*Asian J Surg* 2004;27(4):256-61]

Introduction

The occurrence of breast carcinoma has increased in Japan,[1] and currently, about one in 30 Japanese women will suffer from breast cancer during her life. This increase is mainly due to changes in lifestyle, especially in eating habits, and to the development of mass screening programmes for breast cancer. The detection of early-stage cancers by screening mammography has led to an increasing incidence of non- or early invasive carcinomas. Additionally, recent advances in breast cancer treatment enable us to perform breast-conserving surgery for early-stage cancers.

Pathological analysis of regional lymph nodes is crucial for tumour staging, which is a prognostic indicator.[2] However, total removal of axillary lymph nodes may cause significant morbidity, including limb oedema, loss of sensation and disturbances in limb motion. Sentinel lymph node biopsy (SLNB) is a new trend in breast-conserving surgery. If the sentinel lymph node (SLN) is negative for carcinoma, additional dissection may be avoided, because SLNB is considered a sensitive and specific procedure for predicting regional lymph node status.

General features of lymph node metastases

In Osaka Prefecture, 32% of breast carcinomas were positive for lymph node metastasis in 1996-1998,[3] which is about average in Japan. The proportion of node-positive cancers decreased from 46% in 1975-1977. As nodal involvement is more frequent in larger tumours,[4] the increasing incidence of early-stage cancer may lead to a decrease in the incidence of positive nodes. Many cancers may be truly node negative, but some may be positive with metastatic foci too small to find in routine practice. Multiple sectioning of the lymph nodes for histopathological analysis may improve the detection rate for small metastases.[5] Details of methods for multiple sections or other alternative procedures, as well as their clinical significance, will be discussed later.

Address correspondence and reprint requests to Dr. Takuya Moriya, Department of Pathology, Tohoku University Hospital, 1-1 Seiryo-machi, Aoba-ku, Sendai 980-8574, Japan.
E-mail: moriya@patholo2.med.tohoku.ac.jp • Date of acceptance: 3 November, 2003

© 2004 Elsevier. All rights reserved.

Lymph node metastases mostly occur via lymphatic vessels and, rarely, blood vessels. Small foci of metastatic tumour cells are frequently seen in the subcapsular (marginal) sinus, and these are thought to be the initial evidence of node metastasis. They are either floating within the sinus or attached to the capsule,[6] and may extend to the sinusoids and invade the node parenchyma. Therefore, pathologists must seek the area just beneath the capsule in routine practice if extensive metastases are not seen in low-power view. Additionally, one study suggests a higher probability of metastatic breast carcinoma at the inflow junction of the afferent lymphatic vessels.[7]

Usually, small foci of metastasis do not enlarge the lymph node. However, it is well known that a significant proportion (approximately 20–25%) of clinically node-negative patients will have metastatic foci pathologically.[8] Additionally, negative nodes may show extensive enlargement, caused by accompanying reactive processes such as sinus histiocytosis or reactive hyperplasia of the lymph follicles.

Pathological staging for metastatic carcinoma

Small metastatic foci are currently divided into two categories:[9] isolated tumour cell(s), defined as single cells or small clusters of cells not greater than 0.2 mm in largest dimension, usually floating on the sinus, without any proliferation or stromal invasion and no evidence of malignant activity; and micrometastasis, found in tumour deposits of 0.2–2.0 mm in largest dimension, that may proliferate and destroy the stroma and may have malignant activity. If these small metastases are detected by procedures such as immunohistochemistry or reverse transcriptase-polymerase chain reaction (RT-PCR), they are recommended to note how to detect the metastatic focus.[9] Submicrometastases are metastases that can only be detected by immunohistochemistry and are usually isolated tumour cells.[10] Occult metastases are foci missed by initial screening and identified on subsequent screening, or metastases identified at additional evaluation using paraffin-embedded tissue blocks.[8] Occult metastases are not defined by size but are no larger than micrometastases.

Pathological examination of sentinel lymph nodes

Specimen handling for intraoperative diagnosis

Procedures and guidelines are available for pathological analysis.[4,10] It is strongly recommended that most pathology analysis for SLNs be performed intraoperatively, by frozen-section diagnosis, a combination of frozen section and cytology or supplementary immunohistochemistry, because these results will immediately affect further surgical procedures. Some authors consider that frozen-section diagnosis is not reliable,[11] but it may be effective if technicians and pathologists are well trained and experienced. Frozen-section diagnosis is a safe method, even if radioactive materials are used for SLN detection,[12] as pathologists and technicians suffer only minimal exposure.

In general, as the number of examined slides increases, the rate of detection of micrometastases increases. We believe that one haematoxylin and eosin (H&E)-stained section along the long axis of the node is not sufficient, especially if the node is large. However, serial or step sections across the whole node is time-consuming and costly, and should only be used in research.[13] In routine practice, pathologists should measure the size of the node and then cut it into almost 2 mm thick sections, then perform careful gross examination to detect focal lesions. Cutting along the long axis may be a standard, but it is also possible to cut along the short axis, according to the shape and size of the node. It is desirable that three levels of frozen sections are made for each slice.[10] After surgery, frozen sections should be fixed in formalin and permanent sections made to confirm the intraoperative diagnosis.

Cytology by touch preparation of the cut surface is another procedure for detecting micrometastases. It does not waste tissue by sacrificing for frozen sections and does not suffer from freezing artefacts. It is also easier and faster than frozen-section cutting. However, the evaluation of the specimen is not always easy, and may potentially lead to indeterminate or deferred diagnoses.[4] Pathologists require cytology training, including screening and cell interpretation. The advantages and disadvantages of cytology and frozen-section diagnosis are shown in Table 1.

Accuracy of intraoperative consultation

In SLN analysis, it is very important that pathologists detect metastatic carcinoma accurately. However, the procedure for treating removed node(s) has not been standardized. Therefore, it is not easy to compare different studies to assess the accuracy of each procedure.

The accuracy of frozen-section diagnosis is compared with that of paraffin sections in Table 2.[14–19] Both types of section were evaluated by H&E staining only. There is significant variation in the sensitivity (52–100%) and false-negative rate (0–48%) of frozen-section diagnosis. These discrepancies are probably due to differences in the handling process (including

Table 1. Advantages and disadvantages of frozen section and imprint cytology for intraoperative sentinel lymph node analysis

	Frozen section	Imprint cytology
Advantages	- Interpretation of nodal architecture available - More specific diagnosis possible - Size of metastatic focus measurable - Rapid immunostains available	- Simple/cheap/rapid - Interpretation of cytological/nuclear details available - Avoids tissue loss
Disadvantages	- Relatively time-consuming - More expensive - Freezing artefacts - Tissue loss (by sacrificing)	- Size and area of metastatic focus not detectable - Indeterminate/deferred diagnoses - Need special training to interpret - Sampling error may occur

Table 2. Studies of intraoperative frozen-section diagnosis for sentinel lymph nodes

Authors	No./interval of H&E sections	*N*	Accuracy, %	Sensitivity, %	Specificity, %	False-negative rate, %
Canavese et al (1998)[14]	3 (both sides)	96	96	86	100	14
Schneebaum et al (1998)[15]	Not described	47	98	91	100	9
Koller et al (1998)[16]	3 consecutive	107	83	64	100	36
Imoto et al (2000)[17]	Not described	52	96	89	100	11
Noguchi et al (2000)[18]	2	38	79	60	100	40
Noguchi et al (2000)[18]	> 3	45	93	85	100	15
Noguchi et al (2000)[18]	2 mm interval	26	100	100	100	0
Motomura et al (2000)[19]	1	101	88	52	100	48

H&E = haematoxylin and eosin.

the number and interval of slices, gross inspection and procedures for microscopic slide preparation), and procedures for final pathological evaluation. Other possible influences on the detection rate of metastatic foci are differences in the characters of primary tumours. The size of the primary cancer influences the results of frozen-section diagnosis.[20]

Most metastatic foci missed by frozen-section analysis are either micrometastases or isolated tumour cells. This argues for an awareness that small metastatic foci may be missed at routine intraoperative examination. It is interesting that the specificity of frozen-section diagnosis was 100% in all the studies listed. It is unlikely that trained pathologists will miss foci of carcinomas on microscopic examination. Thus, it is possible that the accuracy of frozen-section diagnosis may be improved either by multiple slices or step/serial sectioning, if the bias due to the skill of the pathologists is ignored. Veronesi and colleagues analysed SLNs by frozen sections every 100–500 μm, but the false-positive rates were 36% and 32% in two studies.[11,21] Therefore, they examined 15 levels of frozen sections at intervals of 50 μm using immunohistochemical analysis. The false-positive rate was reduced to 6%.[11] The accuracy of their last proposal was confirmed by Viale et al.[13] Although this procedure gives good results, it may be too complex and time-consuming for routine practice in most institutions. The significance of immunohistochemistry will be discussed later.

Imprint cytology is compared with permanent H&E-section diagnosis in Table 3. The procedure is quite simple and as accurate as tissue sections. Accuracy and sensitivity are good, and specificity was almost 100%, similar to frozen-section diagnosis.[19,22–26] It is unlikely that benign cells (i.e. histiocytes, lymphocytes) will erroneously be interpreted as carcinoma metastases in most cases. However, we have had some experience of atypical cells on the smear being tentatively described as carcinoma. In such cases, experience is necessary and, if the situation allows, the combination of both frozen section and imprint cytology will be useful.[22]

Multiple levels of H&E sections

The average diameter of ductal carcinoma cells is 20 μm. Theoretically, to detect tumour cell nests of 20–30 cells, it is necessary to make step sections at intervals of 250 μm.[27]

The results of multiple levels of H&E sections are summarized in Table 4. The rate of node-positive patients is increased (4–18% of patients upgraded) by various multiple-section procedures.[28-30] These methods are not always employed at the time of frozen-section diagnosis because they are time-consuming for technicians.

Immunohistochemical analysis of SLNs

As microscopic analysis is somewhat subjective, there are some limitations to detecting metastatic foci on routine staining, even by skillful pathologists. To make examinations more accurate, immunohistochemistry has been used as an adjunct to routine stains, both intra- and postoperatively (Table 5).[30-36] Moreover, if suspicious cells are found on H&E sections, additional immunohistochemistry will be a strong tool for confirmation. Rapid immunohistochemistry using imprint cytology has also been used.[37] Usually, detection of cytokeratin is used in both histology and cytology; 2–20% of patients are upgraded by this procedure. The combination of multiple H&E sections with either single immunohistochemistry or

Table 3. Studies of intraoperative imprint cytology for sentinel lymph node examination

Authors	No./interval of sections	*N*	Accuracy, %	Sensitivity, %	Specificity, %	False-negative rate, %
Moriya et al (1994)[22]	1	286	99	95	100	5
Rubio et al (1998)[23]	1	124	99	96	100	5
Ratanawichitrasin et al (1999)[24]	2	55	98	93	100	7
Motomura et al (2000)[19]	2 mm interval	101	96	91	99	9
Henry-Tillman et al (2002)[25]	> 1	479	99	94	100	6
Karamlou et al (2003)[26]	1	446	-	75	100	5

Results were compared with permanent haematoxylin and eosin sections of the same level; studies with immunohistochemical analysis were eliminated.

Table 4. Studies on multiple levels of haematoxylin and eosin (H&E) sections for sentinel lymph node examination

Authors	*N*	Study design	Patients positive by standard methods, *n* (%)	Patients upgraded by alternative methods, *n* (%)
Turner et al (1999)[28]	52	2 H&Es at 40 μm interval vs additional 2 H&Es at 160 μm interval	10 (19)	2 (5)
Nahrig et al (2000)[29]	40	1 H&E vs 4 additional H&Es at 150 μm intervals	18 (45)	4 (18)
Torrenga et al (2001)[30]	250	1 H&E vs additional 4 H&Es at 250 μm intervals	69 (28)	8 (4)

Table 5. Studies of immunohistochemical staining (IHC) for sentinel lymph node examination

Authors	*N*	Study design	Patients positive by standard methods, *n* (%)	Patients upgraded by IHC, *n* (%)
Czerniecki et al (1999)[31]	41	1 H&E vs 4 levels of IHC	12 (29)	3 (7)
Noguchi et al (1999)[32]	62	1 H&E vs IHC	24 (39)	1 (2)
Pendas et al (1999)[33]	478	1 H&E vs IHC	93 (19)	41 (9)
Kowolik et al (2000)[34]	33	2 H&Es vs IHC	8 (24)	4 (12)
Mann et al (2000)[35]	51	1 H&E vs IHC	10 (20)	10 (20)
Wong et al (2001)[36]	973	1 H&E vs 2 levels of IHC	104 (11)	58 (6)
Torrenga et al (2001)[30]	250	1 H&E vs IHC	69 (28)	5 (2)
Torrenga et al (2001)[30]	250	1 H&E vs 4 levels of IHC	69 (28)	17 (7)

H&E = haematoxylin and eosin.